Effects of the standing accretion-shock instability and the lepton-emission self-sustained asymmetry in the neutrino emission of rotating supernovae

Walk, Laurie; Tamborra, Irene; Janka, Hans-Thomas; Summa, Alexander

Effects of the standing accretion-shock instability and the lepton-emission self-sustained asymmetry in the neutrino emission of rotating supernovae

Laurie Walk and Irene Tamborra

Niels Bohr International Academy and DARK, Niels Bohr Institute, University of Copenhagen,
Blegdamsvej 17, 2100 Copenhagen, Denmark

Hans-Thomas Janka and Alexander Summa

Max-Planck-Institut für Astrophysik, Karl-Schwarzschild-Strasse 1, 85748 Garching, Germany

The rotation of core-collapse supernovae affects the neutrino emission characteristics. By comparing the neutrino properties of three three-dimensional supernova (SN) simulations of a 15 $M_\odot$ progenitor (one nonrotating model and two models rotating at different velocities), we investigate how the neutrino emission varies with the flow dynamics in the SN core depending on the different degrees of rotation. The large-amplitude sinusoidal modulations due to the standing accretion-shock instability are weaker in both the rotating models than in the nonrotating case. The SN progenitor rotation reduces the radial velocities and radial component of the kinetic energy associated with the convection interior to the protoneutron star. This effect seems to disfavor the growth of the hemispheric neutrino-emission asymmetries associated with the lepton-emission self-sustained asymmetry. An investigation of the multipole expansion of the neutrino luminosity and the electron neutrino lepton number flux shows a dominant quadrupolar mode in rotating SN models. Our findings highlight the power of using neutrinos as probes of SN hydrodynamics.

I. INTRODUCTION

Neutrinos are key particles in the yet mysterious core-collapse supernova (SN) explosion mechanism, carrying about 99% of the total explosion energy [1]. According to the delayed neutrino mechanism, neutrinos revive the shock wave stalled in the iron shell which finally triggers the explosion. Hydrodynamical instabilities take place in this phase, enhancing the efficiency of the energy transferred to the shock wave for its revival. In particular, large-scale convective overturns develop in the neutrino-heated postshock layer as well as the standing accretion shock instability (SASI), involving a global deformation and sloshing motion of the shock front.

The advent of high-fidelity SN modeling in three dimensions (3D) has recently begun [1–14]; it has shed new light on the strong directional dependence of the neutrino emission properties [3,15–20]. Notably, a dedicated post-processing of the neutrino emission characteristics from 3D SN simulations, performed with sophisticated neutrino transport, illustrated a significant sensitivity of the neutrino signal to the SASI instability [3,16–18,21]. It was found that the neutrino signal from high-mass progenitors is likely to exhibit imprints of SASI [3,17] in the form of large-amplitude sinusoidal modulations detectable for observers located in the proximity of the SASI plane, even for supernovae (SNe) at the edge of our Galaxy. In particular,

the Fourier power spectrum of the detectable neutrino signal was found to exhibit a clear peak corresponding to the SASI oscillation frequency [17]. On the other hand, low mass progenitors seem to be characterized by pure convective activity which induces small-scale and low amplitude modulations in the neutrino signal not detectable experimentally [3,17].

Three-dimensional simulations with energy-dependent neutrino transport also led to the discovery of the first hydrodynamical instability fostered by neutrinos, the so-called lepton-emission self-sustained asymmetry (LESA) [16]. This surprising phenomenon manifests itself as a macroscopic dipole in the electron neutrino lepton number (ELN) which may have interesting consequences on neutrino flavor conversions, the nucleosynthesis of chemical elements, and the neutron-star radius. LESA has recently been confirmed by large and independent sets of simulations [1,22–25].

Another crucial aspect, potentially affecting the (detectable) neutrino signal, is the progenitor rotation. The role of SN angular momentum is a subject of debate. In particular, rotation has been invoked as a crucial ingredient favoring the SN explosion, potentially affecting the production of *r*-process elements, and determining the pulsar spin period. Rotation is also considered as relevant for the so-called magnetorotational mechanism, according to which magnetic fields are amplified to dynamically relevant strengths

by extremely high spin rates [26–29]. The progenitor rotation also seems to affect the neutrino emission properties [15,19] as well as LESA, which is expected to be damped by progenitor rotation [1].

By relying on the three self-consistent 3D hydrodynamical simulations of a 15 $M_\odot$ SN (a nonrotating model, and two models rotating at different velocities within observational constraints) of Ref. [4], we investigated the possibility of adopting neutrinos as SN gyroscopes in a companion paper [15]. It was concluded that the detectable modulations in the neutrino event rate due to SASI are smeared out by rotation. In particular, fast rotation led to a successful explosion, and long-lasting accretion downflows of matter affected the detectable neutrino signal after the explosion.

By looking at the spectrograms of the detectable neutrino event rate for the three SN models, it was found that rotation is responsible for inducing modulations in the neutrino rate at frequencies higher than the SASI frequency [15]. Such a feature is a discriminant of the progenitor rotation, and it should be detectable for observers located in the proximity of the main SASI plane. On the other hand, if the observer is located away from the SASI plane, degeneracies in the neutrino event rate due to weak SASI modulations and the effects of the progenitor rotation may occur, making it more difficult to determine the progenitor rotational velocity through neutrinos.

In this work, we analyze the phenomenological implications of SN rotation on the neutrino emission characteristics, in particular connected to SASI and LESA features. We stress that, given the complex interplay of the various hydrodynamical instabilities, our work is a first step toward pinpointing the effects of rotation through neutrinos; an in-depth analysis of the consequences of rotation on the hydrodynamic instabilities in SN cores is beyond the scope of the present work. Our study is based on the nonrotating and two rotating 15 $M_\odot$ SN models presented in Ref. [4]. The new results are compared with those obtained for a set of progenitors and their SN simulations presented in previous publications [2,3,16,17].

The structure of the paper is as follows. In Sec. II, we provide essential details of the hydrodynamical simulations of the three 15 $M_\odot$ SN models. In Sec. III the evolution of the neutrino emission characteristics of the studied SN cases is presented, while Sec. IV focuses on characterizing the temporal modulations of the neutrino signal due to hydrodynamical instabilities in the presence and absence of rotation. In Sec. V the effects of rotation on the LESA instability are investigated. Finally, conclusions are presented in Sec. VI. Details on the method adopted in Sec. IV and employed to decouple the effects in the neutrino signal due to SASI from the ones due to LESA are provided in Appendix. Animations of the evolution of the ELN are provided as Supplemental Material [30].

II. HYDRODYNAMICAL SUPERNOVA SIMULATIONS

Details on the three adopted hydrodynamical simulations can be found in Ref. [4]. In this section, key distinguishing features of the SN dynamics in the three simulations are briefly outlined.

All three simulations employ the PROMETHEUS-VERTEX code which includes three neutrino flavors, energy dependent and ray-by-ray plus neutrino transport, as well as state-of-the-art modeling of the microphysics. The simulations were carried out on an axis-free Yin-Yang grid (2 degrees angular resolution for the rotating models and 4 degrees for the nonrotating one). All simulations adopt the Lattimer and Swesty nuclear equation of state with a nuclear incompressibility of 220 MeV.

The nonrotating model shows SASI spiral activity in [120,250] ms after core bounce; SASI then decays as the shock expands after the infall of the Si-SiO interface. This can be seen in the top panels of Fig. 1, which show the evolution of the absolute fluid velocity in the (x, y) plane corresponding to the equatorial plane of the simulation grid (i.e., the plane perpendicular to the rotation axis z for the rotating models) for three selected snapshots chosen at times to be further motivated in Sec. V. A global deformation of the postshock layer in the equatorial plane, caused by the sloshing motions of the SASI instability, is clearly visible.

The slowly rotating model relies on an initial angular velocity profile from stellar evolution calculations including angular momentum transport caused by magnetic fields. The specific angular momentum is 6×10^{13} cm^2 s^{-1} at the Si/SiO interface prior to the core collapse; it has a spin period of 6000 s. As is evident from the panels of the second row of Fig. 1, this model does not exhibit strong SASI signatures. Instead, the convective activity fostered by neutrino heating causes the formation of curl-like currents in the postshock layer.

The fast rotating model is the only simulation of this set which explodes successfully. It has a specific angular momentum of 2×10^{16} cm^2 s^{-1} at the Si/SiO interface in the precollapse state, corresponding to a spin period of about 20 s. The rapid rotation triggers an early SASI spiral mode in the equatorial plane perpendicular to the rotation axis. As a result, a successful explosion occurs around 200 ms postbounce, when the infalling Si-SiO interface reaches the shock wave. The shock wave is then pushed outwards, and, as a consequence, neutrino heating within the gain layer is enhanced. An oblate deformation along the equatorial plane occurs which grows when the successful explosion sets in. The earliest time snapshot of the fast rotating model along the equator in Fig. 1 displays imprints of the SASI spiral motions. The oblate deformation generated by the rapid rotation can be seen in the left bottom panel of Fig. 1 [where the velocity distribution is instead plotted in the (x, z) plane], in the form of increased
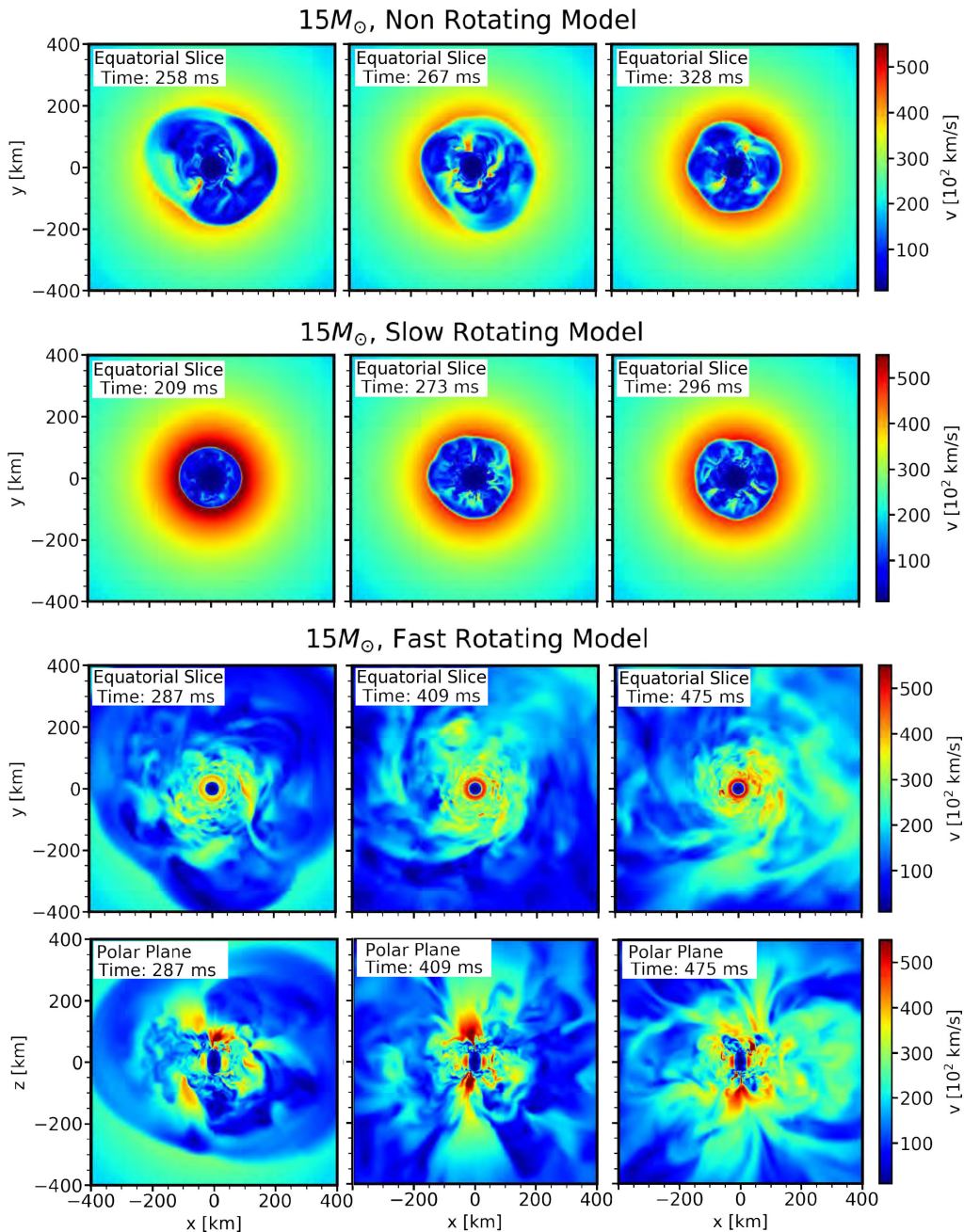
FIG. 1. Cross-sectional slices showing the absolute fluid velocity for the 15 $M_\odot$ nonrotating, slowly rotating, and fast rotating models (from top to bottom), at three different chosen simulation times to be motivated in Sec. V (from left to right). The z axis corresponds to the rotation axis, while the x,y axes span the equatorial plane perpendicular to the rotation axis. The top panels represent the velocity distributions in the (x, y) plane. The polar slices in the bottom panels represent the velocity distributions in the (x, z) plane and are oriented such that the north (south) poles are at the upper half (lower half) of the plots. Imprints of the SASI sloshing motions are clearly visible for the nonrotating SN model, while SASI is weak in the slowly rotating model. The rapidly rotating model explodes by the aid of a strong spiral SASI mode that develops in the (x, y) plane. Unsteady polar downflows of matter accreting onto the PNS affect the postexplosion dynamics of the fast-rotating model and manifestly appear in the polar slices of this case.

rotational velocity close to the protoneutron star (PNS). The panels in the bottom of Fig. 1 also illustrate large-scale funnel-like structures along the rotation axis, which correspond to unsteady polar downflows of matter accreting onto the PNS at postexplosion times.

III. EVOLUTION OF THE NEUTRINO EMISSION PROPERTIES

Neutrinos carry characteristic imprints of the hydrodynamical instabilities and the rotation dynamics which govern each SN model. In this section, we explore these

effects by comparing and contrasting the time evolution of the neutrino properties between the three SN models.

A. Directional neutrino emission properties

The neutrino emission characteristics displayed throughout the rest of this work have been extracted at a radius of 500 km [31] and remapped from the Yin-Yang grid onto a standard spherical grid. The neutrino properties have then been projected to appear as they would for a distant observer at selected angular coordinates, following the procedure outlined in Appendix A of Ref. [3] (see also Ref. [32]). The neutrino emission properties for every angular direction as seen by a distant observer can be provided upon request for all three SN models.

We begin by investigating the dependence of the neutrino properties on the observer direction. Figure 2 shows the neutrino emission characteristics of the non-rotating 15 $M_\odot$ model along directions of strong, intermediate, and weak signal modulations. These directions have been selected by determining the total modulation in each angular zone over the mentioned SASI time interval

relative to the 4π average. Figure 3 of Ref. [15] shows the angular coordinates of the observer directions studied (cf. also Sec. IV therein); note that the selected angular directions refer to the directions where the neutrino signal exhibits the largest overall variation; see Sec. IV A for a related discussion. For each panel, the red, blue, and green curves refer to ν_e, $\bar{\nu}_e$, and ν_x signals, respectively. We denote the nonelectron flavor $\nu_{\mu,\tau}$ by ν_x. For each flavor ν_β, the panels from top to bottom show the neutrino luminosity, mean energy, and pinching factor (α_{ν_β}), respectively. The latter is defined such that [33,34]

$$\frac{\langle E_{\nu_\beta}^2\rangle}{\langle E_{\nu_\beta}\rangle^2} = \frac{2 + \alpha_{\nu_\beta}}{1 + \alpha_{\nu_\beta}}, \tag{1}$$

with $\langle E_{\nu_\beta}\rangle$ and $\langle E_{\nu_\beta}^2\rangle$ being the first and second energy moments.

The nonrotating 15 $M_\odot$ SN model exhibits global neutrino features similar to those observed in other existing simulations of nonrotating SN progenitors; see e.g., Refs. [1,3,16,17]. In fact, the large-amplitude sinusoidal
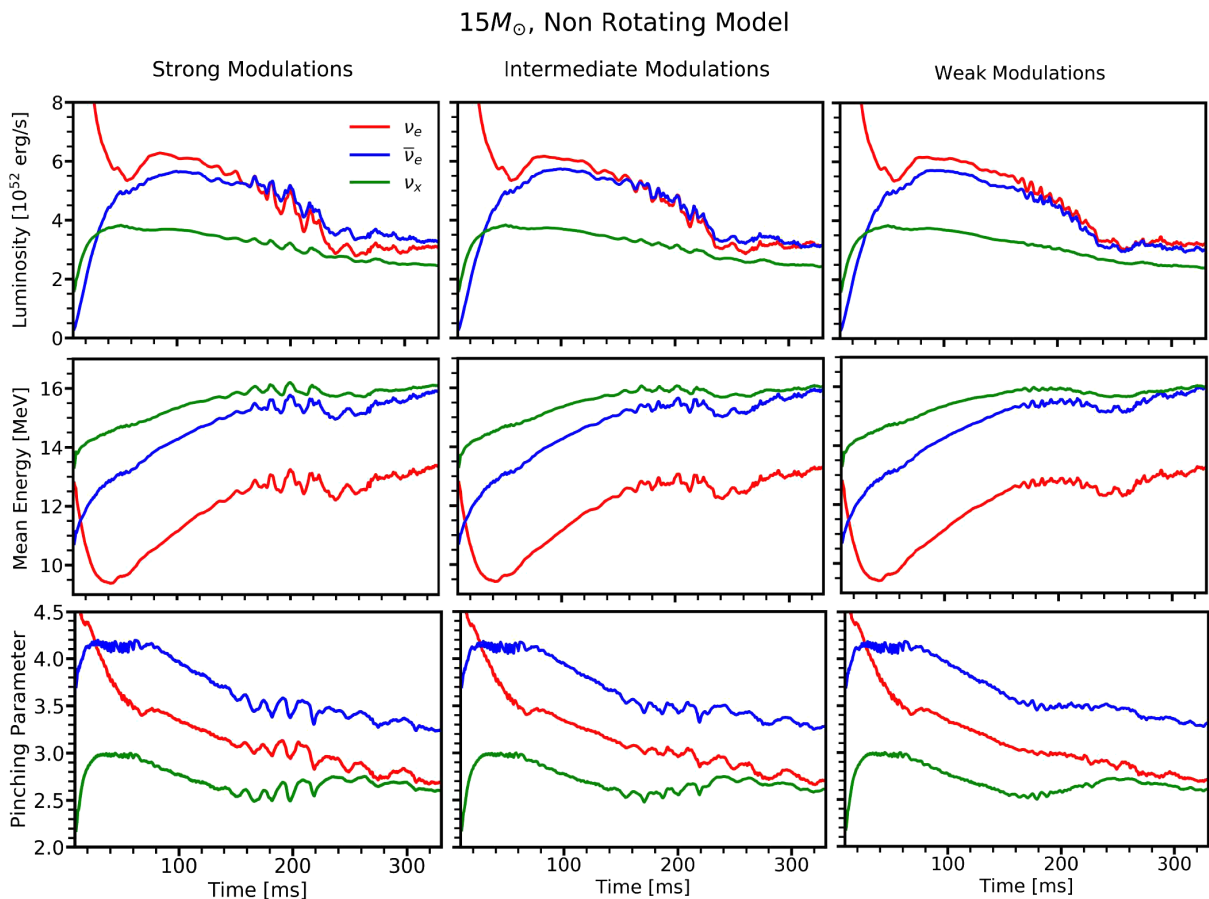

FIG. 2.   Temporal evolution of the neutrino emission properties for the nonrotating 15 $M_\odot$ model as seen by a distant observer. For ν_e, $\bar{\nu}_e$, and ν_x (in red, blue, and green, respectively), the luminosity, mean energy, and pinching parameter are shown from top to bottom. The directions with strong, intermediate, and weak modulations have been chosen according to the directions with the maximum, intermediate, and minimum signal modulation as explained in Sec. IV (Fig. 3) of Ref. [15].

modulations in the neutrino signal due to SASI resemble what is displayed in Fig. 6 of Ref. [3] for a nonrotating $27\,M_\odot$ model. However, although the properties of the $15\,M_\odot$ nonrotating model show comparable SASI signatures, this model exhibits weaker SASI than the 27 and $20\,M_\odot$ models. Evidence for this will be presented and discussed in the following section.

Figure 3 presents the neutrino emission properties for the slowly rotating model. By comparison with Fig. 2, it is immediately apparent that the neutrino properties exhibit weaker amplitude modulations than those of the nonrotating model because of weaker SASI [4]. Additionally, in contrast to the nonrotating case, the amplitude of the modulations increases as the observer plane shifts from the "strong" direction to the direction with "weak" modulations, an effect which is most clearly visible in the luminosity of ν_e in the SASI interval, [120,250] ms. Remarkably, this effect, which may seem counterintuitive at first, is linked to the fact that the quadratic mean square variation, employed to select these observer directions, provides information on the overall strongest modulations, but does not necessarily select the strongest SASI modulations, as will be discussed in Sec. IV. Finally, the properties of the slowly rotating model are significantly less directionally dependent than those of the nonrotating

model, again aiding the idea that global emission asymmetries are damped by rotation.

The corresponding neutrino emission properties of the $15\,M_\odot$ fast rotating model are presented in Fig. 4. Rapid rotation reduces the mass accretion rate of the newly formed neutron star, resulting in lower neutrino luminosities and mean energies compared to those observed in Figs. 2 and 3. After the explosion has set in, long-lasting, unsteady, massive polar downflows occur [15], making the dynamics of this model considerably different from the other two cases. The polar downflows of matter induce small-scale fluctuations in the neutrino emission, which are reflected in the noiselike amplitude modulations embedded in each neutrino signal for times beyond ∼200 ms. These modulations are directionally independent because matter flows between the two poles of the PNS while neutrinos are radiated (see also Fig. 1 of Ref. [15]). At the same time, the rapid rotation pulls matter out along the equatorial plane prior to the explosion and smears out the imprints of the strong SASI activity in the neutrino signal at earlier times. These two effects both contribute to the weak directional dependence of the neutrino emission properties of the fast rotating SN model.

Next, we investigate the effect of rotation on the neutrino luminosity of different neutrino flavors relative
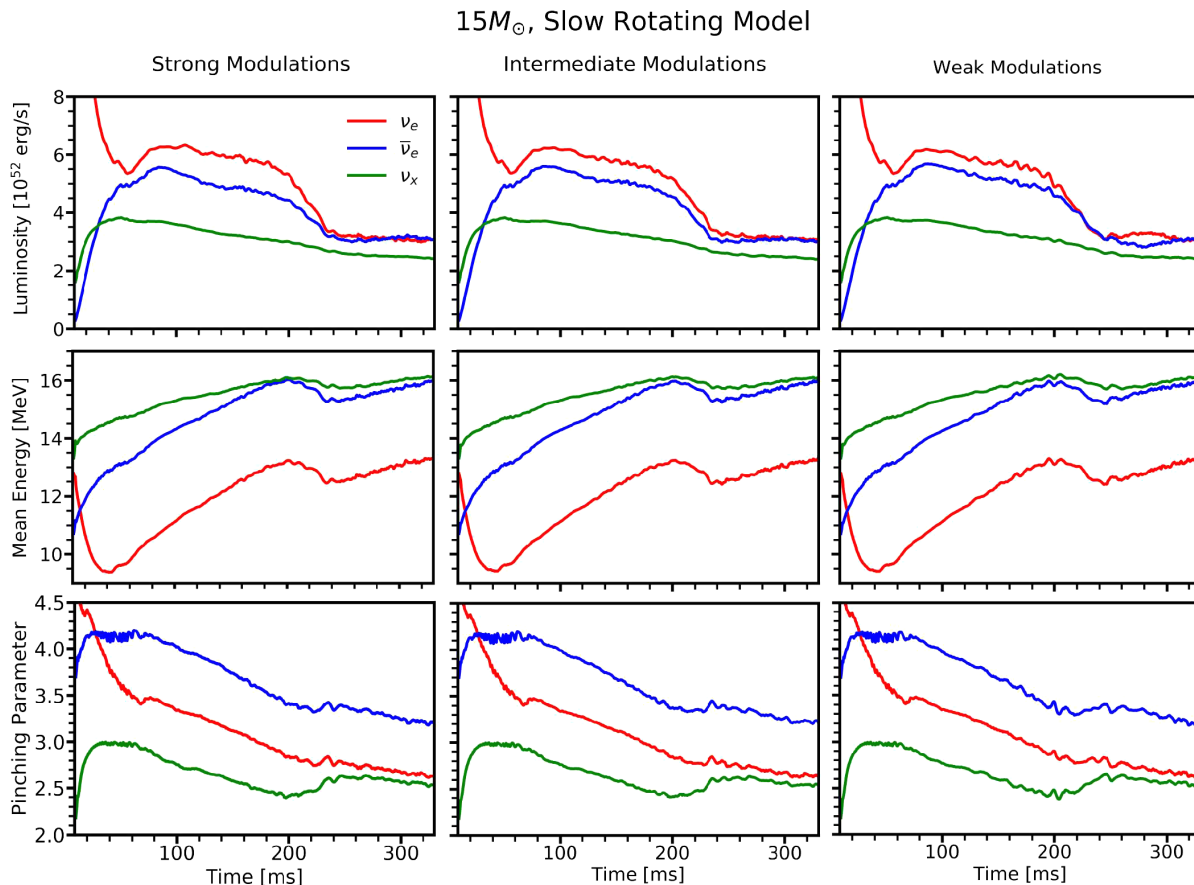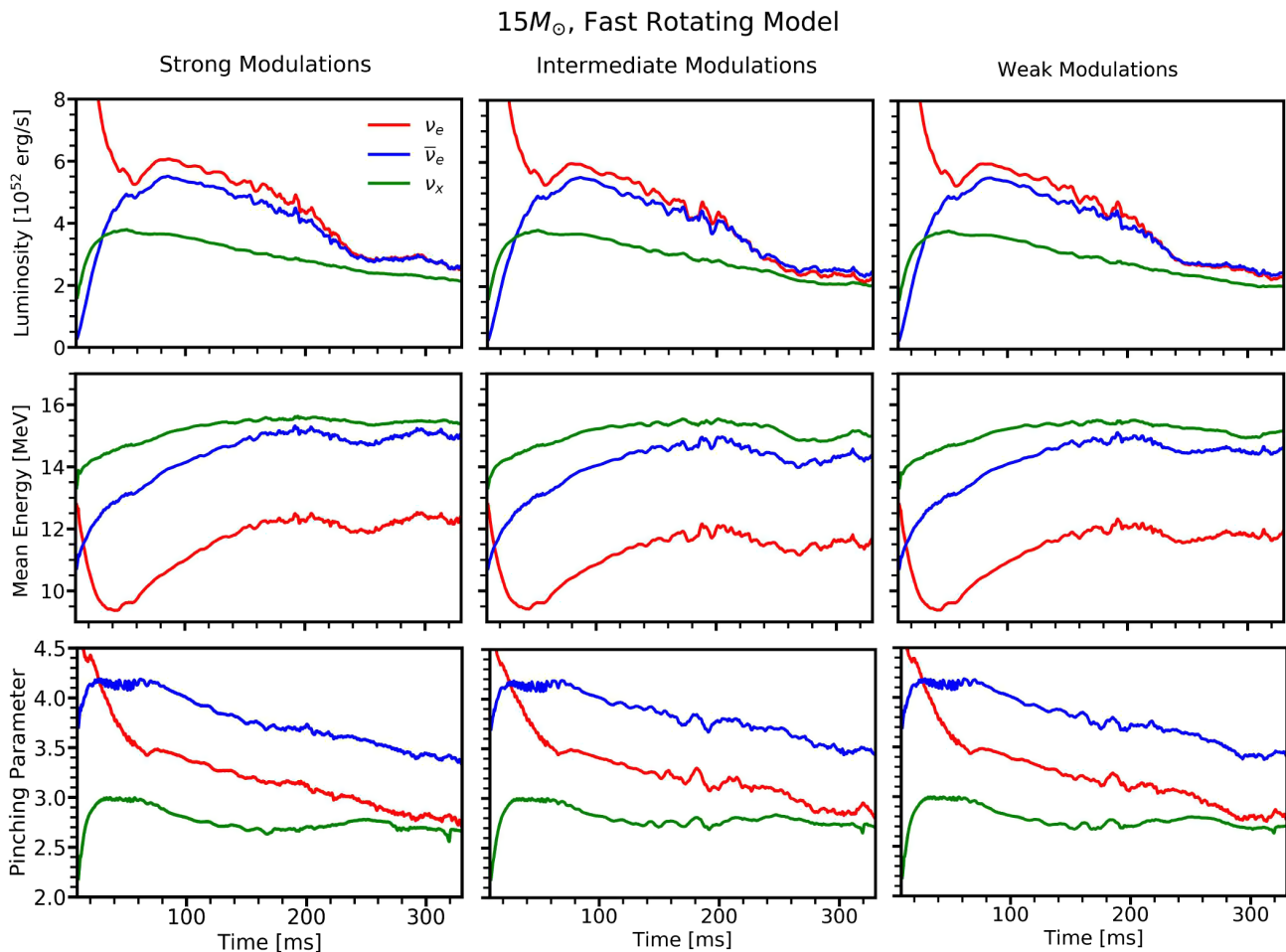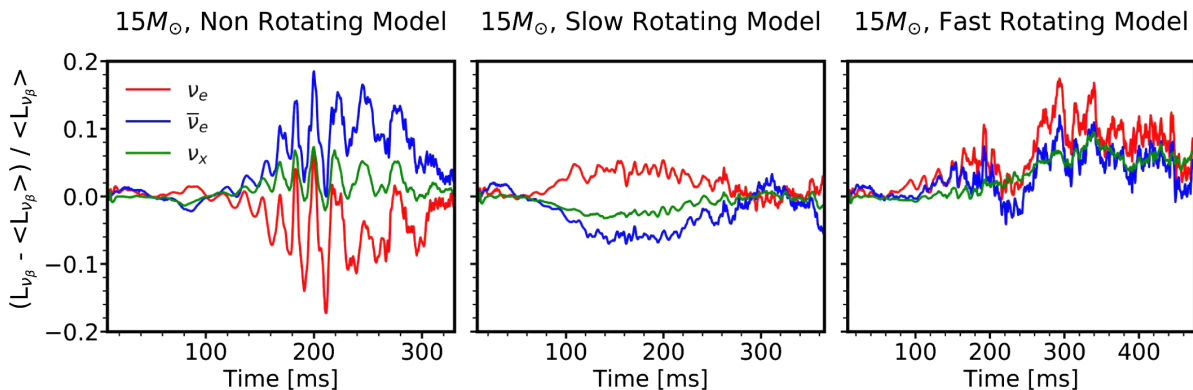
$15M_\odot$, Slow Rotating Model

FIG. 3. Analogous to Fig. 2, but for the slowly rotating $15\,M_\odot$ SN model.

FIG. 4.   Analogous to Fig. 2, but for the fast rotating 15 $M_\odot$ model.

FIG. 5.   Luminosity evolution for the nonrotating, slow rotating, and fast rotating models, respectively, from left to right, for the ν_e, $\bar{\nu}_e$, and ν_x species as seen by a distant observer, relative to the time-dependent average luminosity over all directions ($\langle L_{\nu_\beta} \rangle$). Each luminosity is plotted along the direction of strongest modulation as defined in Sec. IV (Fig. 3) of Ref. [15].

to the time-dependent average luminosity over all directions ($\langle L_{\nu_\beta} \rangle$):

$$\mathcal{L}_{\nu_\beta} = \frac{L_{\nu_\beta} - \langle L_{\nu_\beta} \rangle}{\langle L_{\nu_\beta} \rangle}. \tag{2}$$

Figure 5 shows $\mathcal{L}_{\nu_\beta}$ as a function of time for the non-rotating, slow rotating, and fast rotating models, respectively, from left to right. The relative luminosity is studied along the "strong" modulation observer direction (as selected in Sec. IV and Fig. 3 of Ref. [15]).

In the nonrotating and slowly rotating models, the relative luminosities of ν_e and $\bar{\nu}_e$ exhibit low-frequency variations in opposite directions, superimposed by correlated high-frequency SASI modulations. This implies that the SN may exhibit regions of stronger/weaker ν_e and $\bar{\nu}_e$ emission, corresponding to the LESA instability [16]. Interestingly, the relative difference between ν_e and $\bar{\nu}_e$ decreases between the panels from left to right, suggesting that LESA is weakened by rotation (see Ref. [1]). Notably, the opposite long-time trends between ν_e and $\bar{\nu}_e$ are not apparent in the fast rotating model, because of the effects of rapid rotation. As can be seen in Fig. 3 of Ref. [15], the direction of strongest modulation for the fast rotating model corresponds to the north pole of the simulation grid. Thus, along this direction, all three flavors have positive relative abundance, as matter is accreted onto the PNS near the pole. This motivates a detailed study of the LESA instability in rotating models, which will be presented in Sec. V.

Last, as the rotational speed increases, high-frequency modulations associated with accretion variations become successively more visible in the relative neutrino luminosity $\mathcal{L}_{\nu_\beta}$, as previously observed in Fig. 4 of Ref. [15]. Furthermore, both ν_e and $\bar{\nu}_e$ exhibit modulations in time with greater amplitude than ν_x does, similar to what was reported in Ref. [3].

B. Neutrino energy distribution

We now consider the effect of the SN progenitor rotation on the neutrino energy distribution. It is shown in Refs. [33,34] that the neutrino energy distribution for each flavor can be well approximated by the so-called α fit, given by

$$f_{\nu_\beta}(E) \propto \left(\frac{E}{\langle E_{\nu_\beta}\rangle}\right)^{\alpha_{\nu_\beta}} \exp^{-(\alpha_{\nu_\beta}+1)E/\langle E_{\nu_\beta}\rangle}. \qquad (3)$$

Figure 6 shows the normalized $\bar{\nu}_e$ energy distribution for the three 15 $M_\odot$ SN models, as well as three nonrotating models with 27, 20, and 11.2 $M_\odot$, presented in Refs. [3,17], in the direction of the largest signal modulation. All neutrino spectra are integrated over the time interval [120,250] ms. Besides decreasing the accretion luminosity emitted by neutrinos, rotation also leads to a slightly more pinched energy spectrum than in the non-rotating case; a similar trend is found for the other neutrino flavors as well. Note, however, that this cannot be used as a discriminating feature of rotation, as the dependence of the spectral pinching on the rotational speed is degenerate with variations associated with the progenitor mass.

IV. EFFECTS OF SASI AND LESA EMISSION ASYMMETRIES

In this section, we aim to identify the strength of SASI and LESA on the neutrino emission properties in the three
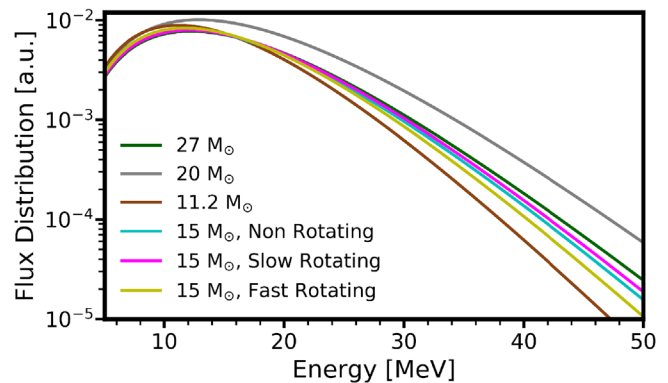

FIG. 6. Energy distribution for the $\bar{\nu}_e$ flavor in arbitrary units as a function of the neutrino energy in the direction of the largest signal modulation and integrated over the time window [120,250] ms (the time interval roughly corresponding to the SASI time window). The neutrino energy distribution for the fast rotating model appears to be more pinched than for the non-rotating and slowly rotating models; however, this feature due to rotation is degenerate with respect to the progenitor mass.

15 $M_\odot$ simulations. In particular, we are interested in exploring whether besides amplitude modulations of the neutrino signal due to SASI, the emission properties also exhibit a spread in their values as a function of the emission angle as a result of LESA. For comparison, we include the 27, 20, and 11.2 $M_\odot$ nonrotating SN models presented in Refs. [3,17].

A. Characterization of direction-dependent variations of the neutrino properties

In Refs. [3,15,17], the root mean squared deviation of the neutrino luminosity in each angular direction from the time-dependent 4π-average luminosity [σ; see Eq. (1) of Ref. [17]] is adopted to estimate the variation in the neutrino emission at each point on the emission sphere. For the 27 and 20 $M_\odot$ models, where SASI is the dominant hydrodynamical instability compared to the other instabilities, the σ parameter was found to be a good quantity to pinpoint the signal modulations coming from SASI directly.

In addition to the amplitude modulations in the neutrino signal arising from SASI, other phenomena such as LESA (discussed in detail in Sec. V) may be at play and may lead to variations of the neutrino properties between different directions. In these cases, the σ parameter may not be an optimal choice to determine directions of strong modulations coming from these different instabilities (see also discussion in Sec. III A). Thus, we introduce two new parameters which help to determine the neutrino luminosity variations due to SASI or LESA exclusively. For simplicity, we focus on the $\bar{\nu}_e$ luminosity, but a similar trend is found for the other neutrino flavors as well.

For each angular direction (θ, ϕ), we begin by defining a time-dependent luminosity $\tilde{L}_{\bar{\nu}_e}(\theta, \phi)$ as the "midline" luminosity found by determining the local maxima and minima of the luminosity signal, and interpolating halfway between them; see Appendix for more details. We then define

$$\Delta = \frac{1}{T} \int_{t_1}^{t_2} dt \left| \frac{L_{\bar{\nu}_e}(\theta, \phi) - \tilde{L}_{\bar{\nu}_e}(\theta, \phi)}{\tilde{L}_{\bar{\nu}_e}(\theta, \phi)} \right|,$$

$$\rho = \frac{1}{T} \int_{t_1}^{t_2} dt \left| \frac{\tilde{L}_{\bar{\nu}_e}(\theta, \phi) - \langle \tilde{L}_{\bar{\nu}_e} \rangle}{\langle \tilde{L}_{\bar{\nu}_e} \rangle} \right|, \quad (4)$$

where $T = (t_2 - t_1)$ and $\langle \tilde{L}_{\bar{\nu}_e} \rangle$ again denotes the time-dependent average of the $\bar{\nu}_e$ luminosity over all directions. For each angular direction, the Δ parameter gives the mean absolute deviation of the luminosity from the corresponding midline luminosity in that same angular direction. This estimates the average variation of the signal amplitude, thus quantifying the effects due to the SASI instability. Contrarily, the ρ parameter gives the mean absolute deviation of the midline luminosity at each angular zone from the 4π average of the midline luminosity. This quantifies the spread in luminosities over all angular emission directions, which is caused by LESA. The parameter Δ can be considered as a measure of the high-frequency neutrino-emission modulations that are characteristic of SASI and convective accretion variations, whereas ρ measures the large-scale emission asymmetries associated with LESA.

Figure 7 shows Molleweide maps of Δ (left) and ρ (right) for the $\bar{\nu}_e$ luminosity. The interval $[t_1, t_2]$ varies between the models as indicated in the figure; the time interval $[t_1, t_2]$ has been chosen to minimize the error in the averaging procedure to determine the midline luminosity that, as discussed in Appendix, lies within the time interval where SASI occurs. As expected, the 27 and 20 $M_\odot$ SN models have the largest Δ modulations as these models have the strongest SASI activity. Although they exhibit some ρ modulations and LESA is present, SASI is clearly the dominant instability affecting the neutrino signal. On the contrary, the 11.2 $M_\odot$ model has no modulation in Δ, and very strong variations in ρ; in fact, it is completely dominated by convection and develops a prominent LESA over time [16].

Interestingly, the 15 $M_\odot$ nonrotating model shows the second highest ρ modulations. It also shows weak SASI activity, indicating that this model experiences effects from both SASI and LESA. In fact, when considering just the four nonrotating models (27, 20, 15, and 11.2 $M_\odot$), a clear trend with respect to SASI dominance as a function of the progenitor mass can be identified. In decreasing SN progenitor mass, the models go from having almost completely SASI dominated activity to an absence of SASI activity, with the 20 and 15 $M_\odot$ models falling in between.
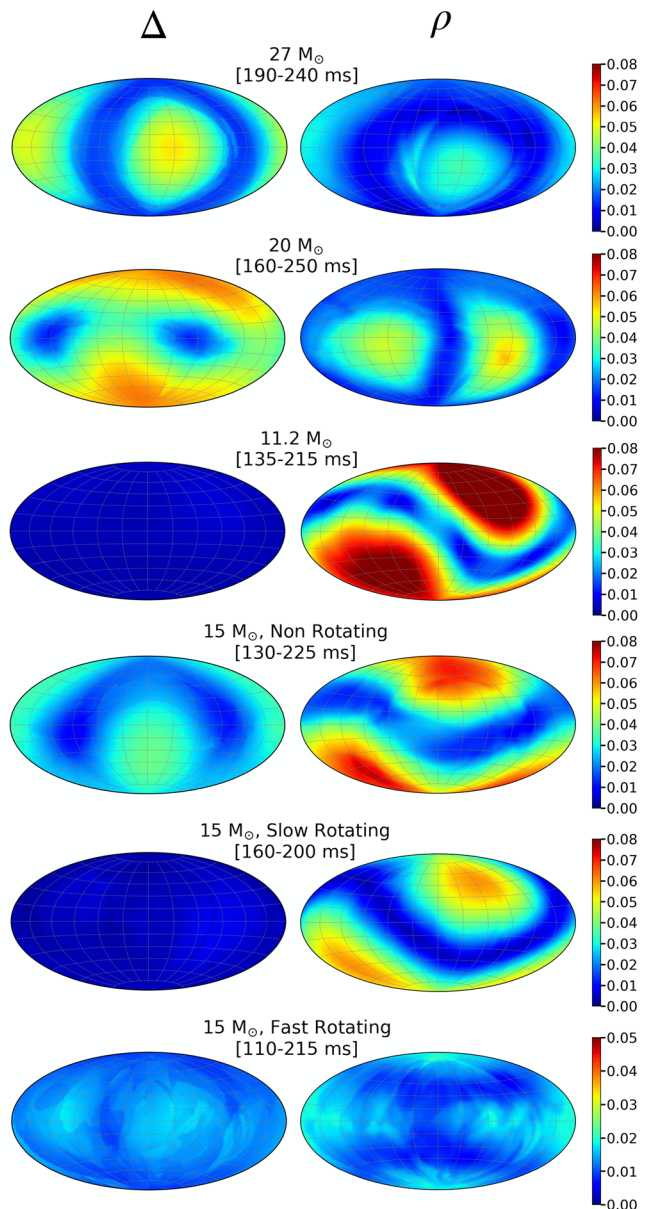

FIG. 7. Molleweide maps of the Δ (left) and ρ (right) modulations as defined in Eq. (4) for the 27, 20, 11.2, and three 15 $M_\odot$ SN models from top to bottom. The chosen time intervals lie within the SASI episode for the models that have SASI ([120,250] ms for the 27, 15, and 11.2 $M_\odot$ models and [150,330] ms for the 20 $M_\odot$ model) and correspond to the interval in which the signal amplitude varies maximally so that the midline interpolation can be found to the highest degree of accuracy. The boundaries of the color bar have been changed for the 15 $M_\odot$ fast rotating model in order to enhance the smaller Δ and ρ modulations in this model compared to the others. The 27 and 20 $M_\odot$ SN models show the largest Δ modulations, these models having the strongest SASI activity. The 11.2 $M_\odot$ model has no modulation in Δ and very strong modulations in ρ, LESA being prominent in this model.

When studying the two 15 $M_\odot$ rotating cases and comparing them to the 15 $M_\odot$ nonrotating model, we see that both the Δ and ρ modulations decrease with

rotational speed. Notably, the fast rotating model shows slightly larger modulations in Δ relative to the slowly rotating model because of variations induced in the neutrino signal by the postexplosion polar downflows of matter. The disappearance of Δ modulations between the nonrotating and slowly rotating models is, again, clear evidence that rotation smears out global SASI neutrino-emission asymmetries, despite the fact that SASI spiral motions are very strong in the fast rotating model.

Rotation decreases the spread in luminosities relative to the 4π-average as well (see also Appendix). This suggests that rotation also disfavors the formation of regions of asymmetric neutrino emission coming from LESA across the surface of the progenitor; this effect was also apparent from Fig. 5; and it fully agrees with the results of LESA presented in Ref. [1].

B. Multipole analysis of the neutrino luminosity

As was apparent from the figures in Sec. III, with increasing rotational velocity, the neutrino-emission modulations due to SASI and/or LESA are weakened. In order to investigate this in more detail, we decompose the luminosity $L_{\bar{\nu}_e}$ into spherical harmonics at the source (i.e., before observer projections) following Refs. [1,35], such that

$$A_l = \sqrt{\sum_{m=-l}^{l} a_{lm}^2}, \quad (5)$$

where

$$a_{lm} = \frac{(-1)^{|m|}}{\sqrt{4\pi(2l+1)}} \int L_{\bar{\nu}_e}(\theta, \phi) Y_l^m(\theta, \phi) d\Omega. \quad (6)$$

The orthonormal harmonic basis functions are

$$Y_l^m(\theta, \phi) = \begin{cases} \sqrt{2} N_l^m P_l^m(\cos\theta)\cos(m\phi) & m > 0 \\ N_l^0 P_l^0(\cos\theta) & m = 0, \\ \sqrt{2} N_l^{|m|} P_l^{|m|}(\cos\theta)\sin(|m|\phi) & m < 0 \end{cases} \quad (7)$$

with

$$N_l^m = \sqrt{\frac{2l+1}{4\pi}\frac{(l-m)!}{(l+m)!}}, \quad (8)$$

where $P_l^m(\cos\theta)$ are the Legendre polynomials. To be consistent with the normalization used in Ref. [16], we normalize the amplitude A_l by $(2l+1)$. According to this formalism, the coefficients a_{11}, a_{1-1}, and a_{10} correspond to the average Cartesian coordinates of $L_{\bar{\nu}_e}$ (x, y, and z, respectively).

Figure 8 shows the $L_{\bar{\nu}_e}$ dipole and quadrupole normalized to the monopole (i.e., $A_{l=1,2}/A_0$) as a function of time.
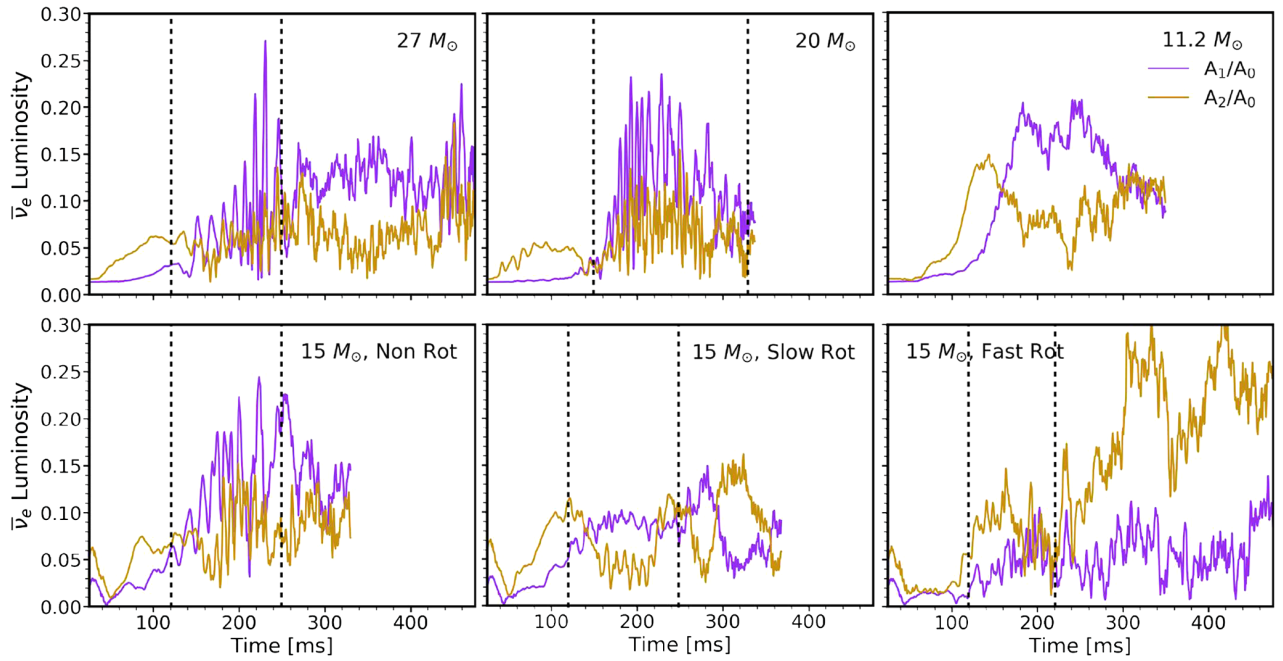

FIG. 8. Time evolution of the dipole and quadrupole strength of $L_{\bar{\nu}_e}$ normalized to the monopole for the 27 ,20, 11.2 and the three 15 $M_\odot$ SN models. The dashed vertical lines mark the SASI interval for each SN model. The $L_{\bar{\nu}_e}$ quadrupole dominates for all models until the beginning of the SASI phase. At later times, the dipole takes over in all of the nonrotating models. Notably, the postexplosion polar accretion flows in the fast rotating model are responsible for the dominance of the quadrupolar mode and its growth at later times.

The $L_{\bar{\nu}_e}$ quadrupole ($l = 2$) dominates for all models until ~120 ms (~150 ms for the 20 $M_\odot$ model), roughly corresponding to the beginning of the SASI phase. This is in agreement with the findings of Ref. [22] which discusses that high l modes (starting with $l = 4$) develop earlier than the low l ones.

At later times, the dipole takes over in all of the nonrotating models. The slowly rotating model experiences periods when the dipole or the quadrupole is dominant; in particular, the slowly rotating model has a dominant dipole moment exactly during the SASI episode because of the SASI shock motions inducing dipolar asymmetries in the mass accretion of the PNS, and thus in the ν_e and $\bar{\nu}_e$ emission. In the case of the rapidly rotating model, instead, the two persistent polar accretion flows are responsible for the dominance of the $L_{\bar{\nu}_e}$ quadrupole mode in the neutrino emission. This is a clear feature associated with the SN rotation.

The 11.2 $M_\odot$ model is a peculiar model because it does not have any SASI activity. In this case, the prominent dipole emission mode visible in Fig. 8 is a pure consequence of LESA (while in all other models the LESA and SASI emission asymmetries are superimposed, both contributing to the dipole). Notably, while the SASI dipoles of all neutrino species are correlated, the LESA dipoles of ν_e and $\bar{\nu}_e$ are anticorrelated and exhibit only long-time variations instead of the higher frequency modulations of the SASI dipole emission [3,16]; see Fig. 5 for both kinds of correlated and anticorrelated behavior between ν_e and $\bar{\nu}_e$.

V. LESA IN ROTATING SUPERNOVA MODELS

In Ref. [16] a large hemispheric asymmetry in the ELN emission (LESA) from the newly formed PNS was discovered in a set of 3D SN simulations based on the ray-by-ray plus approximation. It was found that the dipole amplitude and its direction exhibit a stationary or slowly migrating behavior over time intervals of several hundreds of milliseconds (see Fig. 1 of Ref. [16]). These findings have been confirmed in Ref. [1] in which a larger number of SN models is examined. Independent confirmation of LESA has been presented in Refs. [22–24] recently. These groups have applied a multidimensional transport scheme, providing evidence that LESA is not a numerical artifact arising from the ray-by-ray approximation. In Ref. [22], LESA has been witnessed in a set of eight self-consistent simulations with fully multidimensional and ray-by-ray transport.

As previously seen in Fig. 5, there is a strong anticorrelation between the ν_e and $\bar{\nu}_e$ luminosities in a given angular direction for the nonrotating and slowly rotating models. The magnitude of this anticorrelation seems to decrease with rotation. In this section, we intend to further investigate how LESA affects the neutrino emission properties in the presence of rotation.

A. LESA characterization and multipole analysis

Figure 9 shows a set of snapshots of the ELN flux relative to its 4π average ($(N_{\nu_e} - N_{\bar{\nu}_e})/\langle N_{\nu_e} - N_{\bar{\nu}_e}\rangle$) for each SN model at the source (i.e., before projecting the emitted number flux to a distant observer) to illustrate the evolution of the ELN over time. A strong ELN asymmetry develops in the nonrotating SN model, and the relative strength of this asymmetry decreases with the rotational velocity, whereas only slight asymmetries form at the poles (i.e., perpendicularly to the rotational plane) in the fast rotating model. Animations of the ELN flux evolution on Molleweide maps of the emission surface are provided as Supplemental Material [30] of this paper.

In order to quantify the time evolution of the ELN dipole, we adopt a decomposition in spherical harmonics of the ELN (see Sec. IV B for details). Figure 10 shows the time evolution of the ELN monopole, dipole, and quadrupole ($A_{ELN,0}$, $A_{ELN,1}$, and $A_{ELN,2}$, respectively). The ELN dipole is clearly weakened by the progenitor rotation [1], while the monopole is similar in all three models, as reported in Ref. [16]. Moreover, as the rotational velocity increases, the relative size of the quadrupole grows; the latter fully overtakes the dipole in the fast rotating model. Thus, the ELN multipole decomposition shows a similar pattern to the one shown in Fig. 8, supporting our conjecture that rotation inhibits the development of LESA.

We also examine the time evolution of the ELN dipole axis (corresponding to the LESA dipole in the presence of the LESA instability) in each SN model. The top panels of Fig. 11 track the ELN/LESA dipole direction over a selected time interval. To guide the eye and facilitate a comparison, the location of the positive ELN/LESA dipole direction at the times of the three snapshots in Fig. 9 are marked on each map.

In the nonrotating model, the ELN/LESA dipole stabilizes in the bottom hemisphere in the interval during which the power of the dipole moment is dominant over the quadrupole moment ([150,300] ms from Fig. 10); this is a general trend for nonrotating SN models found in Ref. [16]. For earlier and later times (indicated in Fig. 11 by the darkest and lightest colors, respectively), the quadrupole moment is dominant, and a "sweeping" of the dipole direction over the SN surface is observed.

In the slowly rotating model, we see that the ELN/LESA axis remains in the lower hemisphere, but is dragged over the radiating surface on a path around the rotation axis. This is enhanced in the fast rotating model, where LESA appears to be very weak and the increased rotational speed favors an emission dipole near the equatorial plane. In the fast rotating model, the ELN dipole is comparable to or smaller than the quadrupole during the SASI phase prior to explosion; we suspect that the weak dipole emission is a consequence of the SASI spiral mode and its associated asymmetric PNS accretion, and not to the LESA instability.
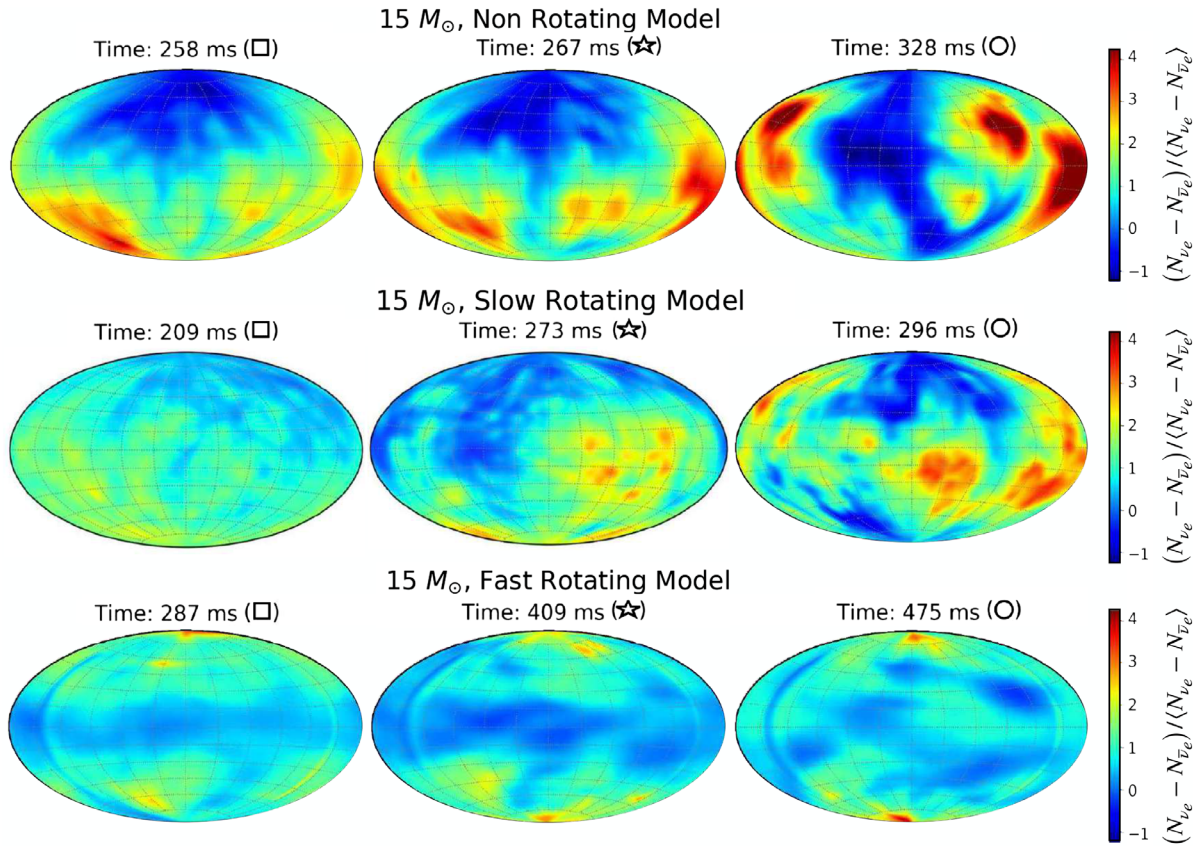
FIG. 9. Snapshots of the ELN flux relative to its 4π average on the emission surface, $(N_{\nu_e} - N_{\bar{\nu}_e})/\langle N_{\nu_e} - N_{\bar{\nu}_e}\rangle$, of the nonrotating, slowly rotating, and fast rotating 15 $M_\odot$ SN models (from top to bottom), respectively. While LESA is visible for the nonrotating model, its evidence becomes weaker as the rotational speed increases. The markers □, ⋆, and ○ are assigned to indicate the first, second, and third time snapshots, respectively.

The interpretation that this phenomenon is *not* identical with the generic appearance of LESA is supported by Fig. 12, where it is shown that the fast rotating model does not exhibit any sign of a hemispheric electron fraction (Y_e) asymmetry inside the convective PNS layer.

The bottom panels of Fig. 11 show the location of the ELN/LESA planes at the times of the three snapshots in Fig. 9. The ELN/LESA plane has been defined as the plane spun by the rotation axis (z axis) and the ELN/LESA dipole axis. The red, green, and blue planes contain the
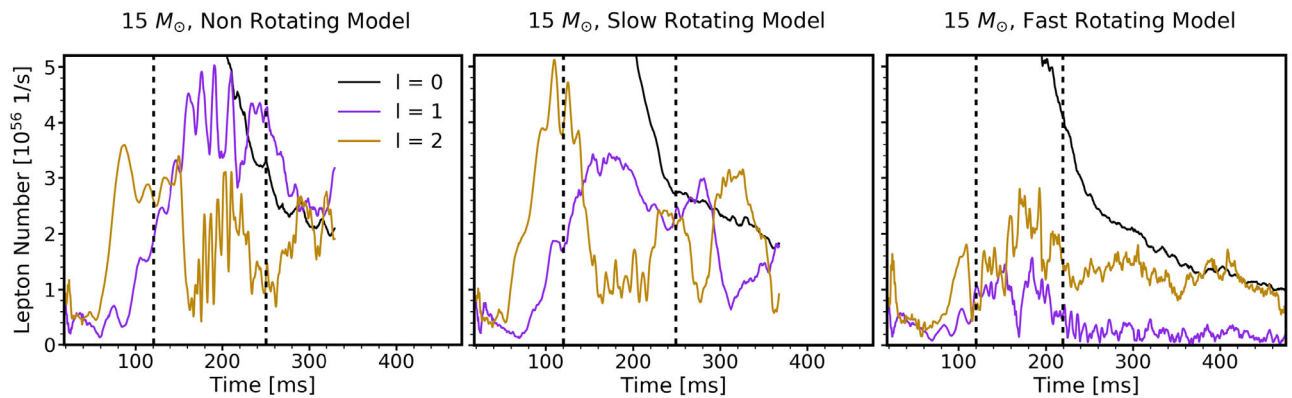

FIG. 10. Time evolution of the monopole (black lines), dipole (purple lines), and quadrupole (gold lines) amplitudes of the ELN emission for the nonrotating, slowly rotating, and fast rotating 15 $M_\odot$ models from left to right, respectively. The dashed vertical lines mark the SASI interval for each SN model. The monopole evolution is similar for all SN models, whereas the dipole amplitude decreases as the rotational velocity increases. A dominance of the quadrupole is observable for the fast rotating model at all times.
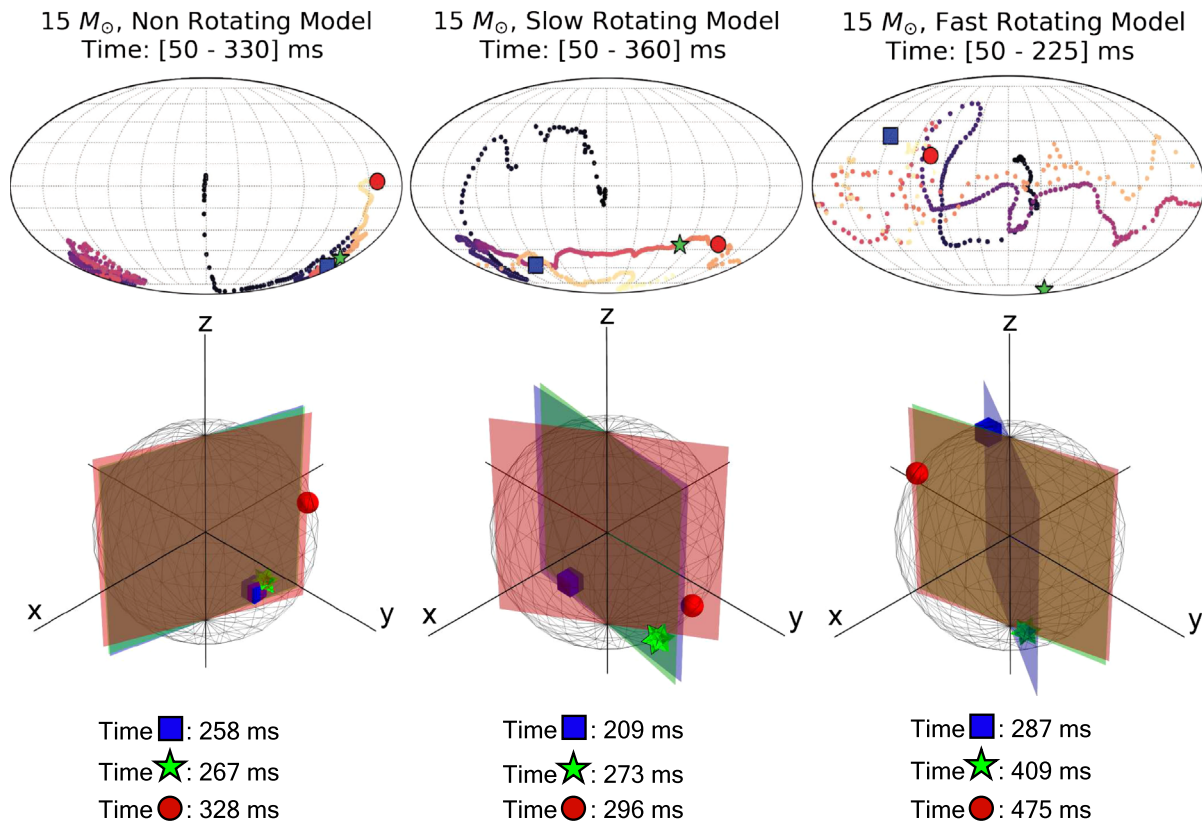
FIG. 11. Top panels: Evolution of the LESA (or ELN) dipole axis for the nonrotating, slowly rotating, and fast rotating 15 $M_\odot$ SN models (from left to right), respectively. The dots mark the path of the positive ELN/LESA dipole direction. The color hues become lighter as time increases. The ELN/LESA axis stabilizes in the bottom hemisphere for the nonrotating model, but is unstable for the fast rotating model. The markers □, ⋆, and ○ are assigned to indicate the positive ELN/LESA dipole moment in the first, second, and third time snapshots as defined in Fig. 9, respectively. Bottom panels: ELN/LESA planes for the nonrotating, slowly rotating, and fast rotating 15 $M_\odot$ SN models (from left to right), respectively, at the snapshot times defined in Fig. 9.

ELN/LESA dipole moment vector, and the rotation axis for the first, second, and third time snapshots, respectively. The location of the positive dipole direction at each time (as indicated on the Molleweide maps in the top panel of the figure) is marked on each plane. For the sake of simplicity, we denote this plane by (x', z), where the x' axis is obtained by projecting the ELN/LESA dipole axis on the (x, y) plane of the grid used for the analysis.

It was shown in Refs. [1,16] that LESA is associated with the formation of a deleptonized region in the direction of the minimal ELN flux, corresponding to a lower electron fraction (Y_e). Figure 12 shows cuts of the spatial distribution of Y_e. In the (x', z) planes containing the ELN/LESA dipole axis (see Fig. 11) and the rotation axis, the plots are oriented such that the north and south poles are at the top and bottom of each plot, respectively. One can see that the nonrotating model develops a clear asymmetry in Y_e, similar to what was observed in Refs. [1,16]. On the other hand, we find that the Y_e distribution becomes more symmetrical as the SN rotational velocity increases, implying that the development of LESA is inhibited.

B. Development of LESA in rotating models

As pointed out in Refs. [36], the strength of convection in rotating and nonrotating SN models is different. In 2D simulations of rotating SNe, it was found that convective activity is confined to the region close to the equator, whereas it involves a whole spherical shell in the corresponding nonrotating model (see Figs. 14 and 11 of Ref. [36]). Since the development of LESA turned out to be strongly connected to the convective activity within the PNS [1,16,22,25], we now investigate whether the suppression of LESA in the rotating models originates from a weakening of the convective overturn within the PNS due to rotation.

In order to test the above conjecture in the presence of SN rotation, Fig. 13 displays the spatial pattern of the fluid velocity at the times of the snapshots in Fig. 9 for the nonrotating, slowly rotating, and fast rotating models from top to bottom, respectively. The spatial distribution is shown in the (x', z) plane defined by the ELN/LESA dipole axis and the SN rotation axis (see Fig. 11). In order to disentangle the convective activity from progenitor inherited or SASI-induced
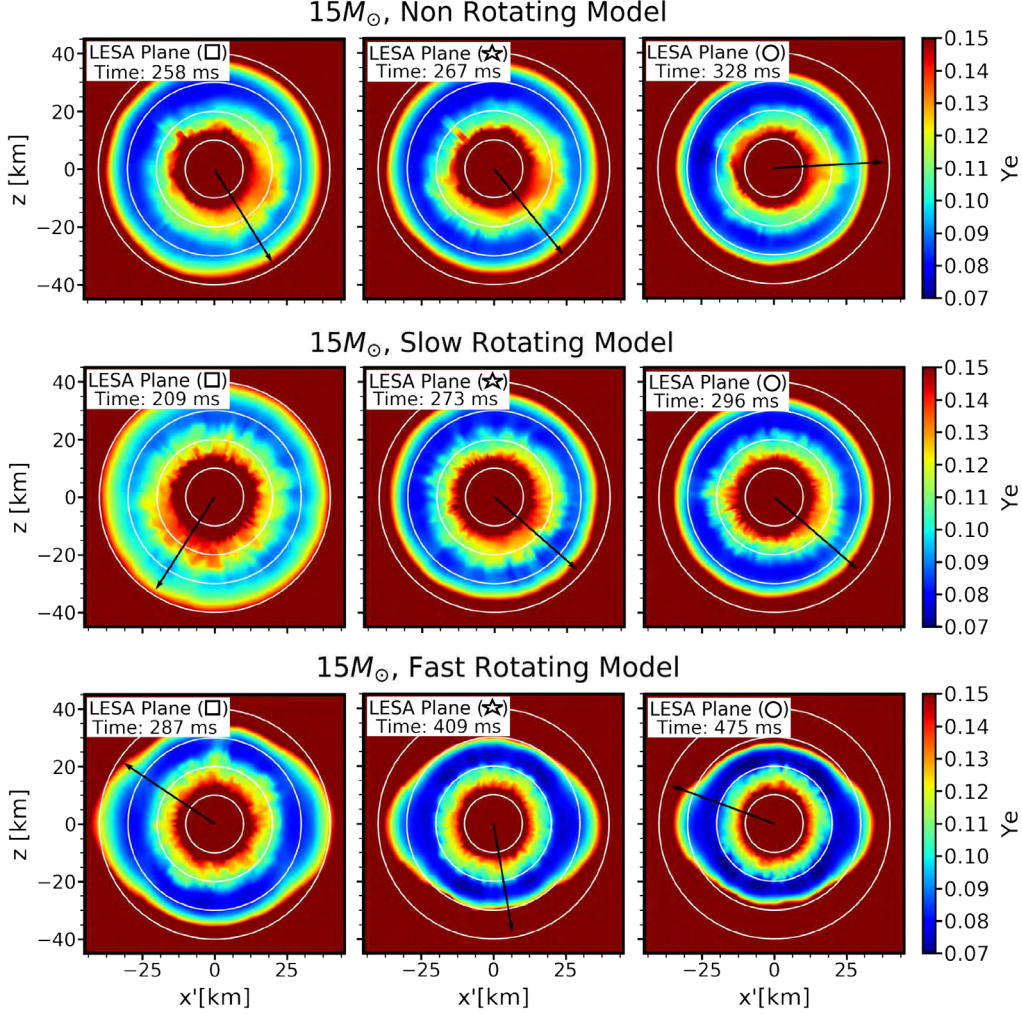
$15M_\odot$, Non Rotating Model

$15M_\odot$, Slow Rotating Model

$15M_\odot$, Fast Rotating Model

FIG. 12.   Slices showing the spatial distribution of the electron fraction, Y_e, inside the PNS, taken at the times of the snapshots in Fig. 9 for the nonrotating, slowly rotating, and fast rotating models from top to bottom, respectively. Each cut is taken along the plane containing the ELN dipole moment vector and the rotational axis (z axis); see Fig. 11. The plots are oriented such that the north and south poles are at the top and bottom, respectively. The black arrows point toward the positive ELN/LESA dipole moment as defined in Fig. 11 by the □, ⋆, and ○ markers for each time snapshot. The white concentric contour lines indicate radii at every 10 km to guide the eye.

rotation of the PNS as well as contraction motion of the PNS, we subtract coherent velocity components from the total fluid velocity. The absolute turbulent velocity is then defined as

$$\mathrm{v} = \sqrt{(v_r - \langle v_r \rangle)^2 + (v_\theta - \langle v_\theta \rangle)^2 + (v_\phi - \langle v_\phi \rangle)^2}, \quad (9)$$

where $v_{r,\theta,\phi}$ are the velocity components along the radial, latitudinal, and azimuthal basis vectors, respectively, computed at each radius and angular zone of the simulation grid. The volume averaged velocity components along r, θ, ϕ ($\langle v_{r,\theta,\phi} \rangle$) are defined as

$$\langle v_r \rangle = \frac{\sum_{\theta,\phi} v_r r^2 \sin\theta \Delta r \Delta\theta \Delta\phi}{4/3\pi(r_3^3 - r_1^3)},$$

$$\langle v_\theta \rangle = \frac{\sum_\theta v_\theta r^2 \sin\theta \Delta r \Delta\theta \Delta\phi}{r^2 \sin\theta \Delta r \Delta\theta \Delta\phi},$$

$$\langle v_\phi \rangle = \frac{\sum_\phi v_\phi r^2 \sin\theta \Delta r \Delta\theta \Delta\phi}{2\pi r^2 \sin\theta \Delta r \Delta\theta}, \quad (10)$$

with Δr, $\Delta\theta$, and $\Delta\phi$ the spacing of the simulation grid with midvalues r, θ, and ϕ, respectively, and $(r_3 - r_1) = \Delta r$, $r_{1,3}$ being the upper and lower radii defining the bin centered on r.

From Fig. 13, one can see that the convective PNS layer is constrained to a narrower shell as time increases, reflecting the PNS contraction. However, the absolute
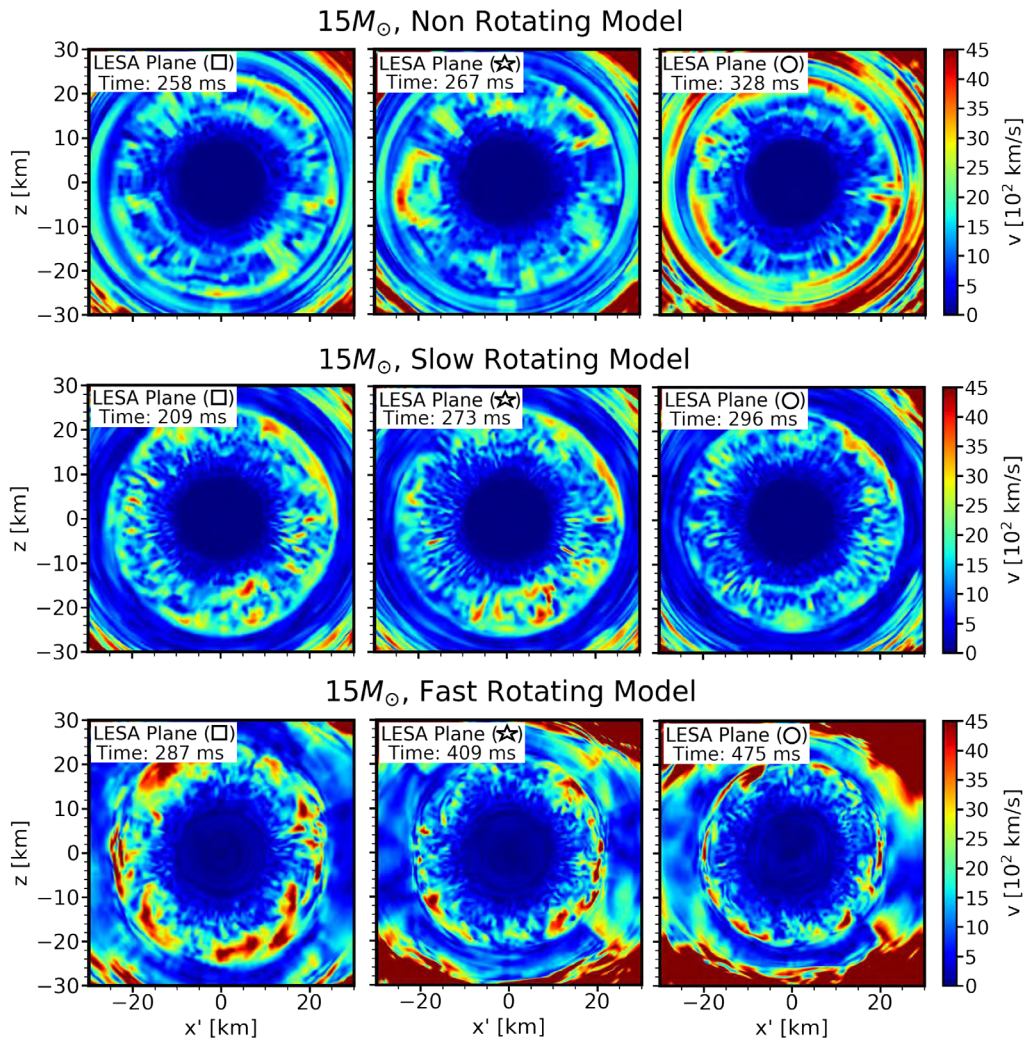
FIG. 13.   Slices showing the spatial distribution of the absolute turbulent velocity of the fluid inside the PNS, as defined in Eq. (9), at the times of the snapshots in Fig. 9 for the nonrotating, slowly rotating, and fast rotating models from top to bottom, respectively. Each cut is taken along the plane containing the ELN/LESA dipole and the rotational axis (see Fig. 11). The plots are oriented such that the north and south poles are at the top and bottom, respectively. The convective activity is confined to a narrower radial layer as the time advances, reflecting the PNS contraction. This is especially visible for the rotating models.

turbulent velocity does not show any clear sign of an eventual weakening of the convective activity as the rotational velocity increases. Therefore, it cannot explain the suppression of the LESA dipole in the fast rotating model. It should also be noted that the LESA direction cannot always be clearly identified in the snapshots of the convective velocities at a single time, given in Fig. 13, because stochastic convective fluctuations can distort the time-averaged picture. Moreover, it is very difficult to subtract rotation effects in a clear way, in particular because massive polar downflows can stir the PNS activity in the fast-rotating model. A conclusive comparison among the three models is also hampered by the fact that the non-rotating model was computed with an angular resolution of 4 degrees in contrast to the resolution of 2 degrees adopted in the two rotating models. Correspondingly, higher

numerical viscosity is likely to damp the convective activity in the nonrotating model.

Convection is driven along the gradient of the gravitational or effective (gravitational and centrifugal for the rotating models) potential, which is dominant in the radial direction. Hence, in order to quantify the effect of rotation on the strength of the LESA instability, we explore the temporal evolution of the turbulent kinetic energy in the PNS convection layer by focusing on its radial component. The radial component of the turbulent kinetic energy in the PNS convection layer is defined as

$$\mathcal{E}_k(t) = \frac{1}{2} \sum_{\theta,\phi} \sum_{r_{\min}}^{r_{\max}} \rho v_r^2 r^2 \sin\theta \Delta\theta \Delta\phi \Delta r, \qquad (11)$$

with $v_r = (v_r - \langle v_r \rangle)$ and $\langle v_r \rangle$ was introduced in Eq. (10). For each time t, the radial component of the turbulent kinetic energy is computed in each angular zone and then integrated over the width of the PNS convection layer. The inner bound of the latter $[r_{\min}(\theta, \phi)]$ is defined by the radius at which the absolute turbulent velocity [Eq. (9)] exceeds 500 km s^{-1}. The outer bound of the PNS convection layer $[r_{\max}(\theta, \phi)]$ is the radius at which the velocity steeply falls, reaching a local minimum between ~ 20 and 25 km (see Fig. 13).

The radial turbulent kinetic energy in the PNS convection layer, $\mathcal{E}_k$, is shown in Fig. 14 as a function of time for the three SN models for $t > 100$ ms postbounce (i.e., when the LESA dipole reaches a significant relative strength; see Fig. 10). A running average over 5 ms bins is used to smooth high-frequency fluctuations and highlight the overall trend. One can see that the rapid rotation is responsible for inducing a reduction of $\mathcal{E}_k$. This, in turn, hints toward a connection between the strength of the LESA dipole and the strength of the radial convective mass motions. Note also that the radial turbulent kinetic energy decreases with time for all models as a result of the PNS contraction.

The strength of LESA in the (non)rotating progenitors can be inferred by investigating the dipole and quadrupole moments of the radial velocity component, v_r, within the
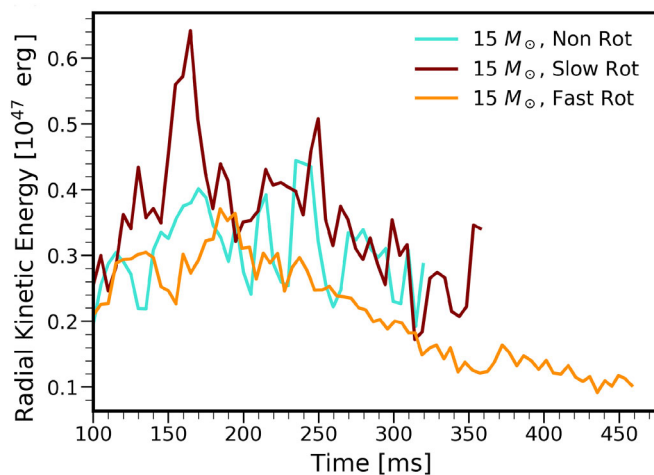

FIG. 14. Radial component of the turbulent kinetic energy in the PNS convection layer as a function of time for the three 15 $M_\odot$ SN models [see Eq. (11)]. The radial component of the turbulent kinetic energy has been averaged over 5 ms bins to smooth short-timescale fluctuations and highlight the overall trend. Only postbounce times later than 100 ms, where the LESA dipole reaches a significant relative strength (see Fig. 10), have been plotted. The radial component of the kinetic energy in the PNS convection layer is reduced in the fast rotating model, implying that the amplitude of the LESA dipole may be linked to the strength of the radial convective mass motions. The clearly decreasing trend in the kinetic energy with time reflects the contraction of the PNS convection layer as time progresses.

PNS (see Refs. [22,25]). Figure 15 shows the amplitudes of the monopole, dipole, and quadrupole moments of v_r for the three 15 $M_\odot$ SN models as a function of radius at each time snapshot given in Fig. 9. The monopole (plotted in black) corresponds to the slow overall contraction of the PNS, and the higher multipoles are components of the mode pattern of the convective motions. These are superimposed in the fast rotating model by effects connected to the rapid rotation, which leads to a time-dependent centrifugal deformation and thus nonvanishing radial velocity components in the convectively stable PNS core and near the PNS surface.

For radii smaller than ~ 25 km, the v_r dipole and the quadrupole are always larger than the monopole. The nonrotating model shows a leading $l = 1$ mode. Instead, in the slow rotating model, the $l = 2$ mode grows between the first and the last considered time snapshots, because rotation has a larger effect at later times. Simultaneously, the $l = 1$ mode decreases in amplitude, although some of the visible relative variations of the dipole and quadrupole may be caused by stochastic fluctuations of the convective activity. In the fast rotating model, the dipole and the quadrupole have comparable amplitudes at small radii ($r \lesssim 10$ km), but the $l = 2$ mode clearly dominates at larger radii for all three snapshots. The nonvanishing low-amplitude activity interior to the convective shell in this model is a consequence of the rotational deformation of the PNS (causing quadrupolar contributions), and of PNS core motion in response to the impact of massive polar accretion downflows (adding a dipolar component).

Comparing the three SN models, one can notice that, as the rotational speed increases, the strength of the dipole of the radial velocity in the PNS decreases, disfavoring the development of the LESA phenomenon. Consequently, dipolar anticorrelation between the ν_e and $\bar{\nu}_e$ luminosities does not arise and the formation of long-lasting hemispheric asymmetries inside the PNS is disfavored. These effects were previously illustrated in Figs. 5, 10, and 12 and confirm that the progenitor rotation inhibits the growth of LESA.

The decrease of the radial component of the turbulent kinetic energy and the reduced strength of the dipole of the radial velocity in the PNS are clearly visible in Figs. 14 and 15 as the rotational velocity increases. We stress that the correlation of this effect of rotation with the reduced LESA amplitude in the rotating models is currently a purely empirical finding. However, the interpretation of LESA as a consequence of the preferred growth of low spherical harmonics modes of the flow in the PNS convective layer would offer a natural explanation (see also Ref. [22]). In fact, the Chandrasekar theory [37] predicts a suppression of the $l = 1$ mode for faster rotation. Since the Taylor number in the PNS convection zone of our fast rotating model is $\mathcal{O}(10^8)$, this should naturally lead to a suppression of the growth of the dipole flow.
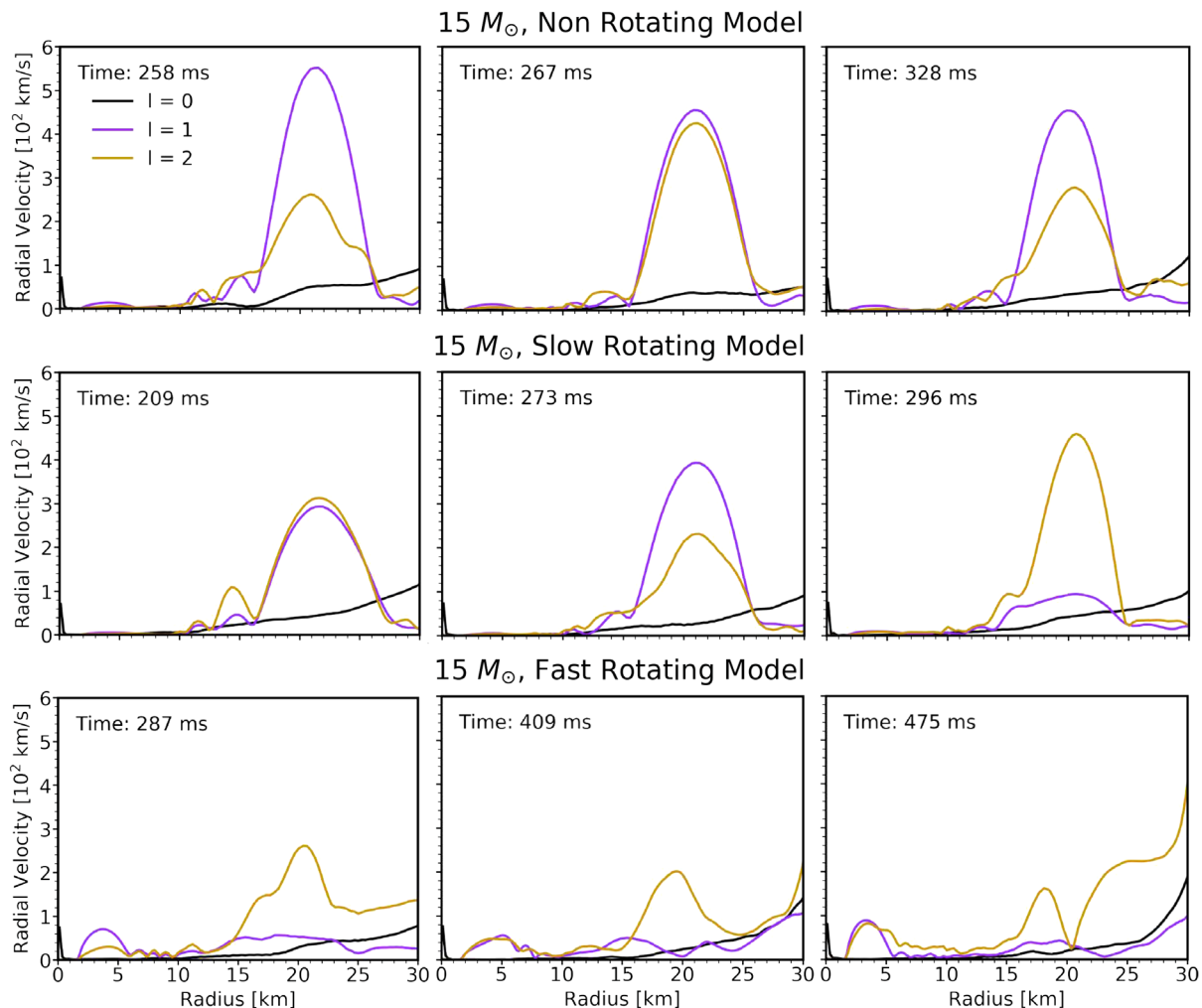
FIG. 15.   Monopole, dipole, and quadrupole amplitudes of the radial component of the velocity, v_r, inside the PNS for the nonrotating, slowly rotating, and fast rotating 15 $M_\odot$ SN models from top to bottom, respectively, for the three time snapshots given in Fig. 9. Intervals with a large dipole moment of v_r in the PNS convection layer correlate with dominant LESA dipoles (see Fig. 10), whereas intervals with a strong or dominant quadrupole of v_r exhibit large quadrupoles of the ELN emission. With an increasing degree of rotation, the strength of convection is damped: the multipole peak of the radial velocity field gets lower, the width of the convective layer tends to shrink (the velocity peak becomes narrower), and a dominant dipolar asymmetry in the case without rotation is replaced by a dominant quadrupolar mode when rotation gets fast. All this is an unambiguous sign that the LESA phenomenon (defined as a dipolar ELN emission asymmetry) is disfavored in the rapidly rotating model because of the strong suppression of the v_r dipole at all radii within the PNS.

The weaker growth and lower amplitude of the LESA dipole for faster rotation in this context require further investigation by future work. This is beyond the scope of the present paper, which primarily aims to identify the imprints of rotation in the neutrino signal.

VI. CONCLUSIONS

Throughout this work we investigated the effects of progenitor rotation on the development of neutrino-emission asymmetries associated with SASI and LESA in core-collapse SNe. Given the nontrivial interplay of the hydrodynamical instabilities, our work is a first attempt to classify the effects of rotation on the development of SASI and LESA through their imprints in the neutrino signal. This study was carried out with three self-consistent models of a 15 $M_\odot$ SN: one nonrotating model and two models with rotational velocities within observational constraints.

The nonrotating model is characterized by a SASI phase imposing large-amplitude sinusoidal modulations on the neutrino emission properties. As a consequence of the SN rotation, the slowly rotating model develops spiral SASI activity that is much weaker than in the nonrotating model, and the neutrino emission properties show modulations with a smaller amplitude than in the nonrotating model. The rapidly rotating model, instead, has a strong spiral

SASI that aids the stellar explosion. Nevertheless, in this last case, the early SASI activity leaves only rather weak imprints on the neutrino signal. The neutrino signal of the fast rotating model, instead, features prominent signatures of the long-lasting polar downflows that develop in the postexplosion phase due to the rapid rotation, and temporal variations hardly depend on the angular location of the observer (see Figs. 4 and 5).

Our findings suggest that the SN progenitor rotation also disfavors the growth of the LESA instability by weakening the convective activity within the PNS along the radial direction. In fact, the radial component of the turbulent kinetic energy in the PNS convection layer is lower when the rotational velocity increases, and the strength of the dipole of the radial component of the fluid velocity inside the PNS decreases. As a consequence, the development of LESA as a dipolar ELN asymmetry is inhibited. This is especially evident in the fast rotating model where we do not observe any sizable anticorrelation between the ν_e and $\bar{\nu}_e$ luminosities (see Fig. 5) nor the LESA-characteristic hemispheric asymmetry of the electron fraction in the deleptonized layer around the PNS convection zone (see Fig. 12). We conclude that the transiently large dipole (between ∼100 ms and ∼200 ms, postbounce) of the lepton number emission (see Fig. 10) in the fast rotating model is a consequence of the strong SASI spiral motions and the corresponding asymmetric PNS accretion. At later stages, after the onset of the explosion in this model, quadrupolar asymmetry dominates the lepton number emission, as well as the luminosities of ν_e and $\bar{\nu}_e$ (see Fig. 8). This can be understood by the accretion luminosity associated with the two polar downflows.

Our results provide empirical evidence that the growth of LESA is interestingly inhibited by progenitor rotation. A quantitative theory of the suppression of convective activity along the radial direction in the PNS and its impact on the development of the LESA phenomenon requires further work. Our findings also show the power intrinsic to the neutrino signal in providing hints on the SN core dynamics. In fact, together with gravitational waves, neutrinos carry imprints of the physics affecting the SN mechanism in the innermost regions not accessible otherwise.

APPENDIX: DIRECTION DEPENDENT VARIATIONS OF THE NEUTRINO EMISSION PROPERTIES

In Sec. IV [Eq. (4)], the Δ and ρ parameters are introduced to disentangle the variations of the neutrino properties due to SASI from the ones due to LESA, i.e., the modulations of the neutrino signal and its spread in intensity between the different angular zones. To that purpose, the time-dependent "midline luminosity" in each angular direction $[\tilde{L}_{\bar{\nu}_e}(t, \theta, \phi)]$ is used to compute the mean absolute modulation amplitude of the time-dependent $\bar{\nu}_e$ luminosity as well as the mean absolute spread in luminosity over a particular time interval.

In this appendix, we outline the interpolation method employed to find $\tilde{L}_{\bar{\nu}_e}(t, \theta, \phi)$, and we illustrate the difference in the Δ and ρ parameters. We use the 27 and 11.2 $M_\odot$ models as examples because they have the most extreme variations of the Δ (27 $M_\odot$) and ρ (11.2 $M_\odot$) parameters (see Sec. IV). For the sake of simplicity, we will focus on $L_{\bar{\nu}_e}$; the luminosity of any other neutrino flavor shows similar trends.

We first select a time window, $[t_1, t_2]$, for which the modulation amplitude of $L_{\bar{\nu}_e}$ is on average the strongest along all angular directions. Then, we determine the local maxima and minima of $L_{\bar{\nu}_e}$ within this time window. For each angular direction, the time-dependent midline luminosity $\tilde{L}_{\bar{\nu}_e}(\theta, \phi)$ is found by first interpolating among all the local maxima and all the local minima, and then by taking the midvalue between the interpolated curves of the minima and maxima at each time step. Figure 16 illustrates this method for the two SN models considered in this appendix. The top panels show the luminosities along the directions of weakest and strongest modulation amplitudes of the neutrino signal. The time window considered is marked with dotted black lines. The bottom two panels show the midline interpolation of each direction for each model within $[t_1, t_2]$.

The Δ parameter is computed for all angular directions by taking the average distance between $L_{\bar{\nu}_e}$ and $\tilde{L}_{\bar{\nu}_e}$ over all time steps in $[t_1, t_2]$. Thus, Δ gives a measure of the mean total modulation amplitude of the neutrino luminosity due to SASI.

The ρ parameter is instead computed by first finding the 4π average of the midline luminosities, $\langle \tilde{L}_{\bar{\nu}_e} \rangle$. Then, we estimate the mean deviation of $\tilde{L}_{\bar{\nu}_e}(\theta, \phi)$ from $\langle \tilde{L}_{\bar{\nu}_e} \rangle$ in $[t_1, t_2]$. Thus, ρ gives an indication of the overall spread in the average neutrino luminosity $L_{\bar{\nu}_e}$ over all directions due to LESA.

Figure 17 shows $L_{\bar{\nu}_e}$ and the corresponding midline luminosities $\tilde{L}_{\bar{\nu}_e}(\theta, \phi)$ with the overall highest (teal) and
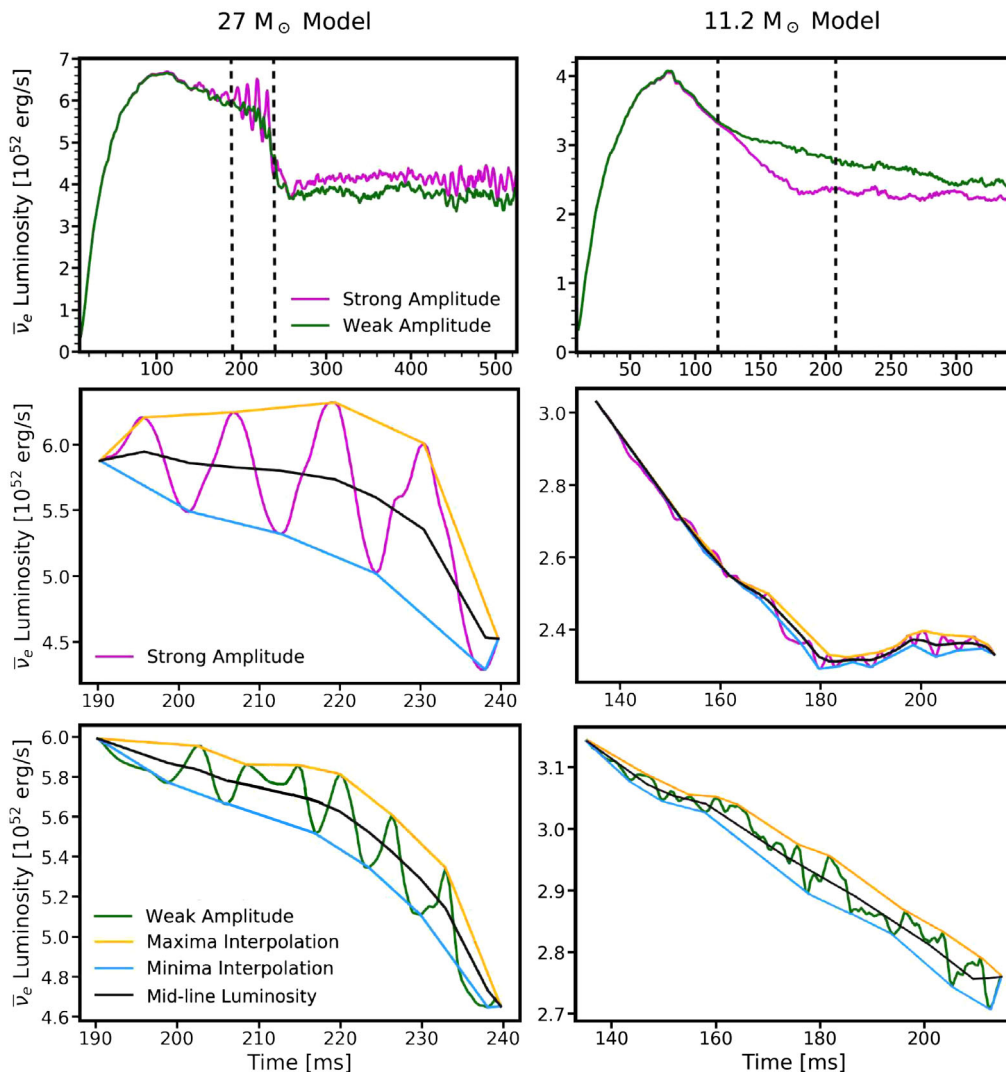
FIG. 16. Representative examples of the method used to find the time-dependent midline luminosity $\tilde{L}_{\bar{\nu}_e}(\theta, \phi)$ for each SN model. The 27 and 11.2 $M_\odot$ models are shown in the panels on the left and right, respectively. Two observer directions corresponding to strong (in magenta) and weak (in green) modulations of $L_{\bar{\nu}_e}$ have been selected. The time interval selected for the interpolation is indicated by dashed black lines (top panels). The midline luminosity obtained is given by the solid black line for the strong (middle panels) and weak (bottom panels) modulation directions.

lowest (magenta) values over angular directions for both SN models, along with the 4π-average midline luminosity $\langle \tilde{L}_{\bar{\nu}_e} \rangle$. From this figure, it becomes clear that in the 11.2 $M_\odot$ model, the distance from the midline luminosity to its 4π average for a particular angular direction is much larger than the average modulation amplitude of the neutrino luminosity for a fixed angular direction, meaning that this model will exhibit strong ρ modulations and relatively low Δ modulations. On the contrary, in the 27 $M_\odot$ model, the magnitude of the amplitude modulations for a fixed angular direction dominates the spread in midline luminosity, such that Δ modulations are dominant.

It should be noted that the interpolation method involves certain approximations. For instance, differentiating local

minima and maxima in the neutrino luminosity due to legitimate physical changes from small-scale noise fluctuations is essential. Because the same maxima/minima parameters are applied to all angular directions, but the size of small-scale fluctuations due to noise may differ between angular directions, there may be instances where the interpolation misses or includes an undesired local minimum or maximum. To minimize the error coming from this effect, we take the integrated average over all times within $[t_1, t_2]$ and apply this at all angular directions. We also stress that $\tilde{L}_{\bar{\nu}_e}$ and $\langle \tilde{L}_{\bar{\nu}_e} \rangle$ are fictitious quantities. They have been introduced only to characterize the spread in the neutrino luminosity between the different angular directions.
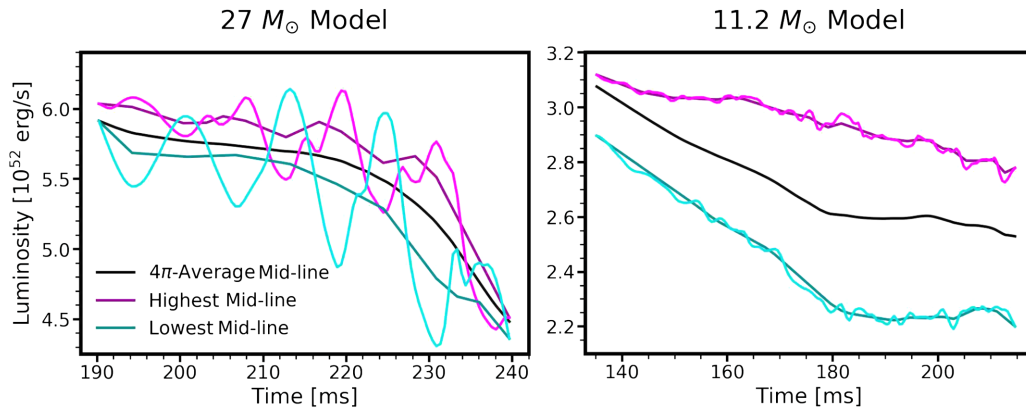
FIG. 17.   Highest average (teal lines), lowest average (magenta lines), and 4π-average (black lines) midline luminosity signals for the 27 and 11.2 $M_\odot$ models from left to right, respectively. Each highest and lowest midline luminosity is embedded in the corresponding luminosity signal. The 27 $M_\odot$ model shows large amplitude (Δ) modulations, while the 11.2 $M_\odot$ model shows a wide spread in the overall neutrino luminosity between different angular directions (ρ).

[1] H.-T. Janka, T. Melson, and A. Summa, Annu. Rev. Nucl. Part. Sci. **66,** 341 (2016).

[2] F. Hanke, B. Müller, A. Wongwathanarat, A. Marek, and H.-T. Janka, Astrophys. J. **770,** 66 (2013).

[3] I. Tamborra, G. G. Raffelt, F. Hanke, H.-T. Janka, and B. Müller, Phys. Rev. D **90,** 045032 (2014).

[4] A. Summa, H.-T. Janka, T. Melson, and A. Marek, Astrophys. J. **852,** 28 (2018).

[5] T. Melson, H.-T. Janka, and A. Marek, Astrophys. J. **801,** L24 (2015).

[6] T. Melson, H.-T. Janka, R. Bollig, F. Hanke, A. Marek, and B. Müller, Astrophys. J. **808,** L42 (2015).

[7] B. Müller, Mon. Not. R. Astron. Soc. **453,** 287 (2015).

[8] B. Müller, Pub. Astron. Soc. Aust. **33,** e048 (2016).

[9] C. Chan, B. Müller, A. Heger, R. Pakmor, and V. Springel, Astrophys. J. **852,** L19 (2018).

[10] T. Takiwaki, K. Kotake, and Y. Suwa, Astrophys. J. **786,** 83 (2014).

[11] T. Takiwaki, K. Kotake, and Y. Suwa, Mon. Not. R. Astron. Soc. **461,** L112 (2016).

[12] B. Müller, T. Melson, A. Heger, and H.-T. Janka, Mon. Not. R. Astron. Soc. **472,** 491 (2017).

[13] E. J. Lentz, S. W. Bruenn, W. R. Hix, A. Mezzacappa, O. E. B. Messer, E. Endeve, J. M. Blondin, J. A. Harris, P. Marronetti, and K. N. Yakunin, Astrophys. J. **807,** L31 (2015).

[14] C. D. Ott, L. F. Roberts, A. da Silva Schneider, J. M. Fedrow, R. Haas, and E. Schnetter, Astrophys. J. **855,** L3 (2018).

[15] L. Walk, I. Tamborra, H.-T. Janka, and A. Summa, Phys. Rev. D **98,** 123001 (2018).

[16] I. Tamborra, F. Hanke, H.-T. Janka, B. Müller, G. G. Raffelt, and A. Marek, Astrophys. J. **792,** 96 (2014).

[17] I. Tamborra, F. Hanke, B. Müller, H.-T. Janka, and G. G. Raffelt, Phys. Rev. Lett. **111,** 121104 (2013).

[18] T. Lund, A. Wongwathanarat, H.-T. Janka, E. Müller, and G. G. Raffelt, Phys. Rev. D **86,** 105031 (2012).

[19] T. Takiwaki and K. Kotake, Mon. Not. R. Astron. Soc. **475,** L91 (2018).

[20] T. Kuroda, K. Kotake, K. Hayama, and T. Takiwaki, Astrophys. J. **851,** 62 (2017).

[21] T. Lund, A. Marek, C. Lunardini, H.-T. Janka, and G. G. Raffelt, Phys. Rev. D **82,** 063007 (2010).

[22] R. Glas, H.-T. Janka, T. Melson, G. Stockinger, and O. Just, Astrophys. J. **881,** 36 (2019).

[23] D. Vartanyan, A. Burrows, D. Radice, M. A. Skinner, and J. Dolence, Mon. Not. R. Astron. Soc. **482,** 351 (2019).

[24] E. O'Connor and S. Couch, Astrophys. J. **865,** 81 (2018).

[25] J. Powell and B. Müller, Mon. Not. R. Astron. Soc. **487,** 1178 (2019).

[26] P. Mösta, S. Richers, C. D. Ott, R. Haas, A. L. Piro, K. Boydstun, E. Abdikamalov, C. Reisswig, and E. Schnetter, Astrophys. J. **785,** L29 (2014).

[27] N. Nishimura, T. Takiwaki, and F.-K. Thielemann, Astrophys. J. **810,** 109 (2015).

[28] M. Obergaulinger and M. Á. Aloy, Mon. Not. R. Astron. Soc. **469,** L43 (2017).

[29] M. Obergaulinger, O. Just, and M. Á. Aloy, J. Phys. G **45,** 084001 (2018).

[30] See Supplemental Material at http://link.aps.org/supplemental/10.1103/PhysRevD.100.063018 for time evolution of the electron neutrino lepton number (ELN) normalized to its average $[(N_{\nu_e} - N_{\bar{\nu}_e})/\langle(N_{\nu_e} - N_{\bar{\nu}_e})\rangle]$ on a Mollweide map of the progenitor's emission surface for the three 15 $M_\odot$ supernova models with different rotational velocities.

[31] The neutrino data in the SN comoving frame have been employed, since any transformation from the comoving frame to lab frame would lead to a negligible correction.

[32] E. Müller, H. T. Janka, and A. Wongwathanarat, Astron. Astrophys. **537**, A63 (2012).

[33] M. T. Keil, G. G. Raffelt, and H.-T. Janka, Astrophys. J. **590**, 971 (2003).

[34] I. Tamborra, L. Hüdepohl, G. G. Raffelt, and H.-T. Janka, Astrophys. J. **839**, 132 (2017).

[35] A. Burrows, J. C. Dolence, and J. W. Murphy, Astrophys. J. **759**, 5 (2012).

[36] H.-T. Janka, K. Kifonidis, and M. Rampp, in *Physics of Neutron Star Interiors*, edited by D. Blaschke, N. K. Glendenning, and A. Sedrakian, Lecture Notes in Physics Vol. 578 (Springer Verlag, Berlin, 2001), p. 333.

[37] S. Chandrasekhar, *International Series of Monographs on Physics* (Clarendon, Oxford, 1961).